



The JWST Early-release Science Program for Direct Observations of Exoplanetary Systems II: A 1 to 20 μm Spectrum of the Planetary-mass Companion VHS 1256–1257 b

Brittany E. Miles^{1,2} , Beth A. Biller³ , Polychronis Patapis⁴ , Kadin Worthen⁵ , Emily Rickman^{6,7} , Kielan K. W. Hoch⁸ , Andrew Skemer¹ , Marshall D. Perrin⁷ , Niall Whiteford⁹ , Christine H. Chen^{10,5} , B. Sargent⁸ , Sagnick Mukherjee¹ , Caroline V. Morley¹¹ , Sarah E. Moran¹² , Mickael Bonnefoy¹³ , Simon Petrus^{14,15} , Aarynn L. Carter¹ , Elodie Choquet¹⁶ , Sasha Hinkley¹⁷ , Kimberly Ward-Duong¹⁸ , Jarron M. Leisenring¹⁹ , Maxwell A. Millar-Blanchaer²⁰ , Laurent Pueyo⁷ , Shrishmoy Ray¹⁷ , Steph Sallum²¹ , Karl R. Stapelfeldt²² , Jordan M. Stone²³ , Jason J. Wang^{24,25} , Olivier Absil²⁶ , William O. Balmer^{5,7} , Anthony Boccaletti²⁷ , Mariangela Bonavita²⁸ , Mark Booth²⁹ , Brendan P. Bowler¹¹ , Gael Chauvin³⁰ , Valentin Christiaens³¹ , Thayne Currie³² , Camilla Danielski³³ , Jonathan J. Fortney¹ , Julien H. Girard⁷ , Carol A. Grady³⁴ , Alexandra Z. Greenbaum³⁵ , Thomas Henning³⁶ , Dean C. Hines⁷ , Markus Janson³⁷ , Paul Kalas^{38,39,40} , Jens Kammerer⁷ , Grant M. Kennedy⁴¹ , Matthew A. Kenworthy⁴² , Pierre Kervella²⁷ , Pierre-Olivier Lagage⁴³ , Ben W. P. Lew⁴⁴ , Michael C. Liu⁴⁵ , Bruce Macintosh⁴⁶ , Sebastian Marino^{47,48} , Mark S. Marley¹² , Christian Marois⁴⁹ , Elisabeth C. Matthews⁵⁰ , Brenda C. Matthews⁵¹ , Dimitri Mawet^{25,52} , Michael W. McElwain⁵³ , Stanimir Metchev⁵⁴ , Michael R. Meyer⁵⁵ , Paul Molliere⁵⁶ , Eric Pantin⁵⁷ , Andreas Quirrenbach⁵⁸ , Isabel Rebollido⁷ , Bin B. Ren¹³ , Glenn Schneider¹⁹ , Malavika Vasist⁵⁹ , Mark C. Wyatt⁶⁰ , Yifan Zhou¹¹ , Zackery W. Briesemeister⁶¹ , Marta L Bryan³⁸ , Per Calissendorff⁶² , Faustine Cantalloube¹⁶ , Gabriele Cugno⁶³ , Matthew De Furio⁶³ , Trent J. Dupuy⁶⁴ , Samuel M. Factor¹¹ , Jacqueline K. Faherty⁹ , Michael P. Fitzgerald⁶⁵ , Kyle Franson^{66,11,77} , Eileen C. Gonzales^{67,68,78} , Callie E. Hood¹ , Alex R. Howe⁶⁹ , Adam L. Kraus¹¹ , Masayuki Kuzuhara⁷⁰ , Anne-Marie Lagrange²⁷ , Kellen Lawson⁷¹ , Cecilia Lazzoni⁷² , Pengyu Liu⁷³ , Jorge Llop-Sayson²⁵ , James P. Lloyd⁷⁴ , Raquel A. Martinez²¹ , Johan Mazoyer²⁷ , Sascha P. Quanz⁷⁵ , Jea Adams Redai⁷⁶ , Matthias Samland⁵⁶ , Joshua E. Schlieder⁶¹ , Motohide Tamura⁷⁴ , Xianyu Tan⁷⁵ , Taichi Uyama³⁵ , Arthur Vigan¹⁶ , Johanna M. Vos⁷⁶ , Kevin Wagner^{19,79} , Schuyler G. Wolff¹⁹ , Marie Ygouf²² , Xi Zhang¹ , Keming Zhang³⁸ , and Zhoujian Zhang¹¹ 

¹ Department of Astronomy and Astrophysics, University of California, Santa Cruz, 1156 High Street, Santa Cruz, CA 95064, USA; bemiles@arizona.edu

² Department of Physics and Astronomy, University of California, Irvine, 4129 Frederick Reines Hall, Irvine, CA 92697-4575, USA

³ Scottish Universities Physics Alliance, Institute for Astronomy, University of Edinburgh, Blackford Hill, Edinburgh EH9 3HJ, UK; Centre for Exoplanet Science, University of Edinburgh, Edinburgh EH9 3HJ, UK

⁴ Institute of Particle Physics and Astrophysics, ETH Zurich, Wolfgang-Pauli-Str. 27, 8093 Zurich, Switzerland

⁵ Department of Physics and Astronomy, Johns Hopkins University, 3400 N. Charles Street, Baltimore, MD 21218, USA

⁶ European Space Agency (ESA), ESA Office, Space Telescope Science Institute, 3700 San Martin Drive, MD 21218, USA

⁷ Space Telescope Science Institute, Baltimore, MD 21218, USA

⁸ Center for Astrophysics and Space Sciences, University of California, San Diego, La Jolla, CA 92093, USA

⁹ Department of Astrophysics, American Museum of Natural History, Central Park West at 79th Street, New York, NY 10024, USA

¹⁰ Space Telescope Science Institute, 3700 San Martin Drive, Baltimore, MD 21218, USA

¹¹ Department of Astronomy, The University of Texas at Austin, Austin, TX 78712, USA

¹² Department of Planetary Sciences, Lunar & Planetary Laboratory, University of Arizona, Tucson, AZ 85721, USA

¹³ Université Grenoble Alpes, Institut de Planétologie et d'Astrophysique (IPAG), F-38000 Grenoble, France

¹⁴ Instituto de Física y Astronomía Facultad de Ciencias, Universidad de Valparaíso, Av. Gran Bretaña 1111, Valparaíso, Av. Gran Bretaña 1111, Valparaíso, Chile

¹⁵ Núcleo Milenio Formación Planetaria—NPF, Universidad de Valparaíso, Av. Gran Bretaña 1111, Valparaíso, Chile

¹⁶ Aix Marseille Univ, CNRS, CNES, LAM, Marseille, France

¹⁷ University of Exeter, Astrophysics Group, Physics Building, Stocker Road, Exeter, EX4 4QL, UK

¹⁸ Department of Astronomy, Smith College, Northampton, MA, 01063, USA

¹⁹ Steward Observatory, University of Arizona, 933 N. Cherry Avenue, Tucson, AZ 85721, USA

²⁰ Department of Physics, University of California, Santa Barbara, CA, 93106, USA

²¹ Department of Physics and Astronomy, University of California, Irvine, 4129 Frederick Reines Hall, Irvine, CA 92697-4575, USA

²² Jet Propulsion Laboratory, California Institute of Technology, Mail Stop 321-100, 4800 Oak Grove Drive, Pasadena CA 91109 USA

²³ Naval Research Laboratory, Remote Sensing Division, 4555 Overlook Avenue SW, Washington, DC 20375 USA

²⁴ Center for Interdisciplinary Exploration and Research in Astrophysics (CIERA) and Department of Physics and Astronomy, Northwestern University, Evanston, IL 60208, USA

²⁵ Department of Astronomy, California Institute of Technology, Pasadena, CA 91125, USA

²⁶ STAR Institute, Université de Liège, Allée du Six Août 19c, B-4000 Liège, Belgium

²⁷ LESIA, Observatoire de Paris, Université PSL, CNRS, Université Paris Cité, Sorbonne Université, 5 place Jules Janssen, F-92195 Meudon, France

²⁸ School of Physical Sciences, Faculty of Science, Technology, Engineering and Mathematics, The Open University, Walton Hall, Milton Keynes, MK7 6AA, UK

²⁹ Astrophysikalisches Institut und Universitätssternwarte, Friedrich-Schiller-Universität Jena, Schillergäßchen 2-3, D-07745 Jena, Germany

³⁰ Laboratoire J.-L. Lagrange, Université Côte d'Azur, CNRS, Observatoire de la Côte d'Azur, F-06304 Nice, France

³¹ STAR Institute, Université de Liège, Allée du Six Août 19c, B-4000 Liège, Belgium

³² Department of Physics and Astronomy, University of Texas-San Antonio, 1 UTSA Circle, San Antonio, TX, USA; Subaru Telescope, National Astronomical Observatory of Japan, 650 North A'ohōkū Place, Hilo, HI 96720, USA

³³ Instituto de Física de Andalucía, CSIC, Glorieta de la Astronomía s/n, E-18008, Granada, Spain

³⁴ Eureka Scientific, 2452 Delmer Street, Suite 1, Oakland CA, 94602, USA

³⁵ IPAC, California Institute of Technology, 1200 E. California Boulevard, Pasadena, CA 91125, USA

³⁶ MPI for Astronomy, Königstuhl 17, D-69117 Heidelberg, Germany

³⁷ Department of Astronomy, Stockholm University, AlbaNova University Center, SE-10691 Stockholm, Sweden

³⁸ Department of Astronomy, 501 Campbell Hall, University of California Berkeley, Berkeley, CA 94720-3411, USA

³⁹ SETI Institute, Carl Sagan Center, 189 Bernardo Avenue, Mountain View CA 94043, USA

- ⁴⁰ Institute of Astrophysics, FORTH, GR-71110 Heraklion, Greece
- ⁴¹ Department of Physics, University of Warwick, Gibbet Hill Road, Coventry, CV4 7AL, UK
- ⁴² Leiden Observatory, Leiden University, P.O. Box 9513, 2300 RA Leiden, The Netherlands
- ⁴³ Université Paris-Saclay, Université Paris Cité, CEA, CNRS, AIM, F-91191, Gif-sur-Yvette, France
- ⁴⁴ Bay Area Environmental Research Institute and NASA Ames Research Center, Moffett Field, CA 94035, USA
- ⁴⁵ Institute for Astronomy, University of Hawai'i, 2680 Woodlawn Drive, Honolulu HI 96822, USA
- ⁴⁶ Kavli Institute for Particle Astrophysics and Cosmology, Stanford University, Stanford California 94305, USA
- ⁴⁷ Jesus College, University of Cambridge, Jesus Lane, Cambridge CB5 8BL, UK
- ⁴⁸ Institute of Astronomy, University of Cambridge, Madingley Road, Cambridge CB3 0HA, UK
- ⁴⁹ National Research Council of Canada
- ⁵⁰ Observatoire de l'Université de Genève, Chemin Pegasi 51, 1290 Versoix, Switzerland
- ⁵¹ Herzberg Astronomy & Astrophysics Research Centre, National Research Council of Canada, 5071 West Saanich Road, Victoria, BC V9E 2E7, Canada
- ⁵² Jet Propulsion Laboratory, California Institute of Technology, 4800 Oak Grove Drive, Pasadena, CA 91109, USA
- ⁵³ Exoplanets and Stellar Astrophysics Laboratory, NASA Goddard Space Flight Center, Greenbelt, MD 20771, USA
- ⁵⁴ Western University, Department of Physics & Astronomy and Institute for Earth and Space Exploration, 1151 Richmond Street, London, Ontario N6A 3K7, Canada
- ⁵⁵ Department of Astronomy, University of Michigan, 1085 S. University, Ann Arbor, MI 48109, USA
- ⁵⁶ Max-Planck-Institut für Astronomie, Königstuhl 17, D-69117 Heidelberg, Germany
- ⁵⁷ IRFU/DAP Département D'Astrophysique CE Saclay, Gif-sur-Yvette, France
- ⁵⁸ Landessternwarte, Zentrum für Astronomie der Universität Heidelberg, Königstuhl 12, D-69117 Heidelberg, Germany
- ⁵⁹ STAR Institute, Université de Liège, Allée du Six Août 19c, B-4000 Liège, Belgium
- ⁶⁰ Institute of Astronomy, University of Cambridge, Madingley Road, Cambridge, CB3 0HA, UK
- ⁶¹ NASA Goddard Space Flight Center, Greenbelt, MD 20771, USA
- ⁶² Department of Astronomy, University of Michigan, 1085 S. University, Ann Arbor, MI 48103, USA
- ⁶³ Department of Astronomy, University of Michigan, Ann Arbor, MI 48109, USA
- ⁶⁴ Institute for Astronomy, University of Edinburgh, Royal Observatory, Blackford Hill, Edinburgh, EH9 3HJ, UK
- ⁶⁵ University of California, Los Angeles, 430 Portola Plaza Box 951547, Los Angeles, CA 90095-1547, USA
- ⁶⁶ Department of Astronomy and Carl Sagan Institute, Cornell University, 122 Sciences Drive, Ithaca, NY 14853, USA
- ⁶⁷ Astrobiology Center of NINS, 2-21-1, Osawa, Mitaka, Tokyo, 181-8588, Japan
- ⁶⁸ NASA-Goddard Space Flight Center, 8800 Greenbelt Rd, Greenbelt, MD 20771, USA
- ⁶⁹ University of Exeter, School of Physics and Astronomy, Stocker Road, Exeter, EX4 4QL, UK
- ⁷⁰ SUPA, Institute for Astronomy, Royal Observatory, University of Edinburgh, Blackford Hill, Edinburgh EH9 3HJ, UK; Centre for Exoplanet Science, University of Edinburgh, Edinburgh EH9 3HJ, UK
- ⁷¹ Department of Astronomy, Cornell University, Ithaca NY 14850, USA
- ⁷² ETH Zurich, Institute for Particle Physics & Astrophysics, Wolfgang-Pauli-Str. 27, 8093 Zurich, Switzerland
- ⁷³ Center for Astrophysics | Harvard & Smithsonian, 60 Garden Street, Cambridge, MA 02138, USA
- ⁷⁴ The University of Tokyo, 7-3-1 Hongo, Bunkyo-ku, Tokyo 113-0033, Japan
- ⁷⁵ Atmospheric, Ocean, and Planetary Physics, Department of Physics, University of Oxford, UK
- ⁷⁶ Department of Astrophysics, American Museum of Natural History, Central Park West at 79th Street, NY 10024, USA

Received 2022 September 3; revised 2022 November 29; accepted 2022 November 30; published 2023 March 22

Abstract

We present the highest fidelity spectrum to date of a planetary-mass object. VHS 1256 b is a $<20 M_{\text{Jup}}$ widely separated ($\sim 8''$, $a = 150$ au), young, planetary-mass companion that shares photometric colors and spectroscopic features with the directly imaged exoplanets HR 8799c, d, and e. As an L-to-T transition object, VHS 1256 b exists along the region of the color–magnitude diagram where substellar atmospheres transition from cloudy to clear. We observed VHS 1256 b with JWST's NIRSpec IFU and MIRI MRS modes for coverage from 1 to $20 \mu\text{m}$ at resolutions of ~ 1000 – 3700 . Water, methane, carbon monoxide, carbon dioxide, sodium, and potassium are observed in several portions of the JWST spectrum based on comparisons from template brown dwarf spectra, molecular opacities, and atmospheric models. The spectral shape of VHS 1256 b is influenced by disequilibrium chemistry and clouds. We directly detect silicate clouds, the first such detection reported for a planetary-mass companion.

Unified Astronomy Thesaurus concepts: [Brown dwarfs \(185\)](#); [Exoplanet atmospheres \(487\)](#); [Extrasolar gaseous giant planets \(509\)](#)

Supporting material: data behind figure

1. Introduction

The light observed from an exoplanet contains information about the planet's composition, atmospheric dynamics, and

other bulk physical properties. This, in turn, can be used to infer how the planet formed and evolved. Various parts of the planet's spectrum contain different information (e.g., Burrows et al. 1997; Kirkpatrick 2005). For example, in a ~ 1000 K gas-giant exoplanet or a more massive brown dwarf analog, the visible part of the spectrum ($<1 \mu\text{m}$) contains alkali lines that can constrain metallicity and surface gravity (Burgasser et al. 2003); the near-infrared part of the spectrum (1 – $5 \mu\text{m}$) contains water (H_2O), carbon monoxide (CO), and methane (CH_4) absorption bands that can constrain atomic ratios (e.g., C/O, C/H, O/H) and turbulent mixing (Barman et al. 2011; Konopacky et al. 2013); and the mid-infrared part of the

⁷⁷ NSF Graduate Research Fellow.

⁷⁸ 51 Pegasi b Fellow.

⁷⁹ NASA Hubble Fellowship Program–Sagan Fellow.



Original content from this work may be used under the terms of the [Creative Commons Attribution 4.0 licence](#). Any further distribution of this work must maintain attribution to the author(s) and the title of the work, journal citation and DOI.

spectrum ($>5 \mu\text{m}$) contains a solid-state silicate feature that can be used to measure the compositions of clouds (Cushing et al. 2005; Suárez & Metchev 2022). The full wavelength range constrains the temperature–pressure profile of the atmosphere and the muting and reddening effects of clouds (Marley et al. 2013).

JWST provides our first opportunity to explore the spectra of brown dwarfs and exoplanets over their full luminous range (Rigby et al. 2022). Previously, the longest-wavelength exoplanet images available were taken at $5 \mu\text{m}$ (e.g., Hinz et al. 2010; Galicher et al. 2011; Morzinski et al. 2015; Rajan et al. 2017), while eclipse measurements of transiting planets have occasionally extended to photometry and spectroscopy out to $24 \mu\text{m}$ (e.g., Knutson et al. 2008; Charbonneau et al. 2008; Grillmair et al. 2008). JWST can measure exoplanet spectral energy distributions (SEDs) with multiwavelength photometry and spectroscopy from 0.6 to $28.1 \mu\text{m}$, a range that contains essentially 100% of the energy emitted by a 300 K exoplanet and 99.6% of the energy emitted by a 1000 K exoplanet (based on models from Morley et al. 2014; Marley et al. 2021).

The Early Release Science (ERS) Program, High Contrast Imaging of Exoplanets and Exoplanetary Systems with JWST (ERS 1386, PI Hinkley), employs several different modes of JWST appropriate for studying directly imaged exoplanets, planetary-mass companions, and the circumstellar disks in which they form (Hinkley et al. 2022). From a technical perspective, the program has been designed to assess the performance of the Near-Infrared Camera (NIRCam) and Mid-Infrared Instrument (MIRI) coronagraphic modes as well as the Near InfraRed Imager and Slitless Spectrograph (NIRISS) aperture-masking interferometry mode with the goal of preparing the community for ambitious direct imaging surveys in Cycle 2 and beyond.

Beyond understanding JWST’s technical performance, the program also aims to provide template spectra of exoplanet atmospheres over JWST’s full wavelength range and improve our understanding of gas-giant atmospheric physics and chemistry (Hinkley et al. 2022). In the high-contrast regime, JWST uses coronagraphs in NIRCam and MIRI to suppress light from an exoplanet’s host star (Green et al. 2005; Krist et al. 2009; Boccaletti et al. 2015, 2022). Both of these modes are imaging only—JWST’s spectroscopic modes do not work with coronagraphy. However, in order to provide the best possible spectral template observations, the High Contrast Imaging of Exoplanets and Exoplanetary Systems with JWST program elected to use the Near-Infrared Spectrograph (NIRSpec) and MIRI integral field spectrographs (Wells et al. 2015; Böker et al. 2022) to observe a widely separated planetary-mass companion,⁸⁰ where coronagraphy is not necessary: VHS J125601.92–125723.9 b (hereafter VHS 1256 b). When selecting targets, our team searched for an object with the following characteristics: (1) a planet-like spectrum, (2) a wide separation and low contrast with its host star so that it could be observed with integral field spectroscopy

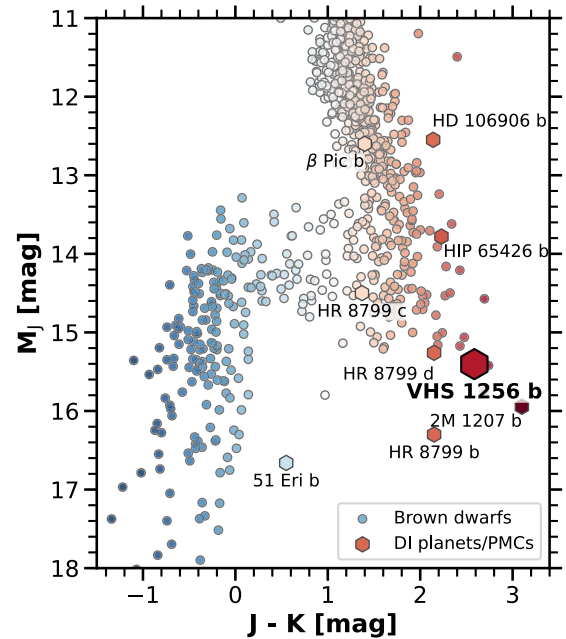


Figure 1. VHS 1256 b (red hexagon) is an analog to directly imaged exoplanets like the HR 8799 planets due to similar near-infrared colors. VHS 1256 b and other directly imaged exoplanets maintain these colors compared to similar-temperature brown dwarfs because of lower surface gravities, which allow clouds to linger in the upper atmosphere. Photometry from <http://bit.ly/UltracoolSheet>.

instead of coronagraphic imaging, and (3) no overlap with the Guaranteed Time Observation (GTO) programs. Among the potential targets considered, VHS 1256 b best fulfilled these requirements.

VHS 1256 b was discovered by Gauza et al. (2015) $\sim 8''$ (~ 150 au) away from an M-dwarf binary (Stone et al. 2016; Rich et al. 2016). Spectra of the host M-star binary and the planetary-mass companion are both consistent with youth ($\lesssim 300$ Myr); the companion has red colors and a triangular H -band feature that is seen in other low-mass companions, as well as weak alkali lines (Gauza et al. 2015; Petrus et al. 2023). The photometry (Gauza et al. 2015) and distance (22.2 pc; Dupuy et al. 2020) of VHS 1256 b place it in the vicinity of other faint red directly imaged planets, such as HR 8799 cde (Marois et al. 2008, 2010) and 2MASS 1207 b (Chauvin et al. 2004) in a color–magnitude diagram (see Figure 1). This distribution of redder photometric colors is theorized to be the result of cloudy atmospheres (Currie et al. 2011; Skemer et al. 2011; Madhusudhan et al. 2011; Skemer et al. 2012; Marley et al. 2012), which can linger in the upper atmospheres of young brown dwarfs, due to low surface gravities being prevalent among the lowest-mass young brown dwarfs (Liu et al. 2016; Faherty et al. 2016).

Spectroscopic, near-infrared studies of VHS 1256 b show absorption from H_2O and CO like other L-to-T transition brown dwarfs, but no CH_4 despite cool effective temperatures that could produce that molecule (Hoch et al. 2022; Petrus et al. 2023). Additionally, VHS 1256 b’s L -band spectrum shows weaker absorption compared to older field brown dwarfs (Miles et al. 2018), which is an indication of disequilibrium chemistry that is also apparent in the spectral energy distributions of the HR 8799 planets (Barman et al. 2011; Skemer et al. 2014). VHS 1256 b does not belong to a known moving group (Gauza et al. 2015; Dupuy et al. 2020), and therefore, at the time it was

⁸⁰ As discussed in Dupuy et al. (2022) and later in this paper, VHS 1256 b’s mass is either just above or just below the deuterium-burning limit that is often used as a dividing line between exoplanets and brown dwarfs. Its formation mechanism is unknown, although its wide orbital separation suggests that it did not form like a typical exoplanet. Depending on its true mass and other context, VHS 1256 b could correctly be referred to as an exoplanet or brown dwarf. Similar to Dupuy et al. (2022), we adopt the intermediate-term, planetary-mass companion.

selected for the JWST program, its age and mass were uncertain. More recently, Dupuy et al. (2022) have determined a system age of 140 ± 20 Myr, based on the measured dynamical mass and bolometric luminosity of the inner binary combined with Baraffe et al. (2015) evolutionary models, confirming VHS 1256 b’s youth and $<20 M_{\text{Jup}}$ mass.

After VHS 1256 b was chosen as an ERS target, Bowler et al. (2020) discovered that it has the largest known variability amplitude of any L dwarf. Later, Zhou et al. (2022) determined that VHS 1256 b has the largest known variability amplitude of any brown dwarf (38% peak to peak at the J band, separated by 2 yr). This variability is potentially caused by heterogeneous temperature and cloud distributions that may be particularly prevalent in the atmospheres of young, low-mass planets (Apai et al. 2013, 2017; Vos et al. 2019; Zhou et al. 2020; Apai et al. 2021; Vos et al. 2022). Therefore, our team has embarked on a campaign to study the object’s variability with ground-based telescopes, which will be published in a subsequent paper. Some of our variability observations are nearly contemporaneous with the JWST-ERS 1386 NIRSpec and MIRI observations. Based on these observations, in Section 6 we constrain the impact of variability on the flux calibration of our spectra during the epoch of our JWST observations.

In this paper, we analyze the ERS 1386 observations of VHS 1256 b, spanning $0.97\text{--}28.1 \mu\text{m}$. Due to JWST’s broad wavelength coverage, spectacular sensitivity, and freedom from telluric absorption, these data are the highest quality ever published for an exoplanet or brown dwarf to date. In Section 2, we describe the JWST observations. In Section 3, we describe our data reduction and present a $0.97\text{--}19.8 \mu\text{m}$ spectrum of VHS 1256 b. In Section 4 we identify features from molecular absorption due to gaseous species and from cloud species. In Section 5, we perform forward-model comparisons to understand atmospheric properties such as disequilibrium chemistry driven by atmospheric mixing and the influence of clouds on VHS 1256 b’s spectral energy distribution. Lastly, in Section 6 we discuss the object’s luminosity, the effect of VHS 1256 b’s intrinsic variability on our data, and the impact of the JWST spectrum on our understanding of the properties of directly imaged exoplanets.

2. Observations

Spectroscopic observations of VHS 1256 b were obtained using NIRSpec and MIRI on JWST. NIRSpec observations were acquired from UT 09:43:42 to 11:48:08 on 2022-07-5. NIRSpec was used in IFU mode to measure a spectrum of VHS 1256 b between 0.97 and $5.27 \mu\text{m}$ at resolutions of $\sim 1000\text{--}2700$, with the following filter/grating combinations: G140H/F100LP, G235H/F170LP, and G395H/F290LP. Each NIRSpec observation with a given filter/grating combination used the full detector with the NRSIRS2RAPID readout and a four-point dither box pattern ($0''.4$ on a side), for a total exposure time of 2144.57 s per filter/grating combination. Over about 1.5 hr, the sequential order of the NIRSpec observation modes were G235H/F170LP and G395H/F290LP, followed by G140H/F100LP with 9 minutes of downtime between each observation mode. MIRI observations were acquired from UT 11:56:54 to 13:56:05 on 2022-07-5. The MIRI observations of VHS 1256 b were completed in the short, medium, and long grating settings of all four IFU channels for overlapping coverage from 4.98 to $28.1 \mu\text{m}$ with a resolution of $\sim 1300\text{--}3000$ using four-point dithering. We

obtained an observation in each MIRI grating/channel mode with the FASTR1 readout setting and total exposure times of 1576.22 s. Channels 1 and 2 had their short, medium, and long observations taken first, then Channels 3 and 4 using the short, medium, and long gratings. An overview of the observations taken is provided in Tables 1 and 2.

3. Spectroscopic Reduction

3.1. JWST/NIRSpec

Version 1.7.2 of the standard JWST pipeline was used to reduce each science observation dither into spectral cubes for the NIRSpec IFU data set. The CRDS versions and context used by the JWST pipeline were “11.16.12” and “jwst_0977.pmap”, respectively. At the time of the initial analysis, the NIRSpec pipeline used instrument parameters determined from ground-based testing (Rigby et al. 2022). Residual bad pixels and cosmic rays remain in the standard pipeline reductions, and these issues are compounded when dithers are reduced together. Each dither was processed through Stage 1, which performs detector-level corrections and converts detector ramps into slope images. After Stage 1, the Stage 2 step removes other instrument artifacts and creates calibrated slope images. Stage 3 of the pipeline takes slope images to create three-dimensional spectral cubes of a target. Total errors are propagated through all stages of the JWST Pipeline starting with variances estimated in the slope-fitting step in Stage 1. Stage 3 spectral cubes have an associated error array with the same dimensions of the spectral cube.

The cube-building step in Stage 3 was run with outlier detection turned off and all parameters set to default values to produce three-dimensional spectral cubes that are aligned in right ascension and declination. The Stage 3 spectral cubes were used to create one-dimensional spectra using aperture extraction. First, the spectral cube for each dither is collapsed along the wavelength axis to calculate a mean image to mitigate the effects of cosmic rays, then a 2D Gaussian is fit to the source point-spread function (PSF) to find the source’s center position. The center of the source’s position changes on a subpixel level in both the x and y directions of the image cube for all NIRSpec observation modes. The source center oscillates as a function of wavelength by $0.2\text{--}0.3$ pixels in the x direction and $0.15\text{--}0.2$ pixels in the y direction. For each image along the spectral cube wavelength axis, we then extract the flux within a circular aperture centered on this position. We tested several extraction radii to find where the object’s flux plateaus with extraction radius. Based on this, we adopted extraction radii of $3\text{--}4$ pixels ($1.2\text{--}1.7$ FWHM) for VHS 1256 b, while the calibrator star required a radius of 4 pixels across all bands. Aperture correction was not applied to the NIRSpec IFU data and it is not relevant for a well-centered point source. The same aperture used for each image is applied to the error array for every wavelength to calculate the error with standard error propagation. The weighted mean of the dithers is taken to produce a final spectrum.

Before a final weighted average is calculated, a hard cutoff is applied to fluxes that are 10% higher than the spectral energy distribution of the initial median to remove wavelengths affected by cosmic rays. Edges of the reconstructed IFU data cube include spatial elements that are not fully illuminated, and the extracted spectra derived from these parts of the data cube are removed from the final spectrum. After the cutoffs are

Table 1
Observations of VHS 1256 b with JWST

Instrument	Mode	Wavelength	Subarray	Readout	Resolving Power	Exposure Time (s)
NIRSpec	G140H/F100LP	0.97–1.89	FULL	NRSIRS2RAPID	~1000	1283.82
NIRSpec	G235H/F170LP	1.66–3.17	FULL	NRSIRS2RAPID	~2700	1283.82
NIRSpec	G395H/F290LP	2.87–5.27	FULL	NRSIRS2RAPID	~2700	1283.82
MIRI	Channel 1, Short A	4.9–5.74	FULL	FASTR1	3320–3710	1576.22
MIRI	Channel 1, Medium B	5.65–6.63	FULL	FASTR1	3190–3750	1576.22
MIRI	Channel 1, Long C	6.53–7.65	FULL	FASTR1	3100–3610	1576.22
MIRI	Channel 2, Short A	7.51–8.76	FULL	FASTR1	2990–3110	1576.22
MIRI	Channel 2, Medium B	8.67–10.15	FULL	FASTR1	2750–3170	1576.22
MIRI	Channel 2, Long C	10.01–11.71	FULL	FASTR1	2860–3300	1576.22
MIRI	Channel 3, Short A	11.55–13.47	FULL	FASTR1	2530–2880	1576.22
MIRI	Channel 3, Medium B	13.29–15.52	FULL	FASTR1	1790–2640	1576.22
MIRI	Channel 3, Long C	15.41–18.02	FULL	FASTR1	1980–2790	1576.22
MIRI	Channel 4, Short A	17.71–20.94	FULL	FASTR1	1460–1930	1576.22
MIRI	Channel 4, Medium B	20.69–24.44	FULL	FASTR1	1680–1770	1576.22
MIRI	Channel 4, Long C	23.22–28.1	FULL	FASTR1	1630–1330	1576.22

Notes. Breakdown of the early-release science observations of VHS 1256 b completed for our program. Both JWST/NIRSpec and JWST/MIRI utilized 4four-point dithering over the exposure. Resolution values for each of the instrument modes are from the following websites: NIRSpec (<https://jwst-docs.stsci.edu/jwst-near-infrared-spectrograph/NIRSpec-observing-modes/NIRSpec-ifu-spectroscopy>) and MIRI (<https://jwst-docs.stsci.edu/jwst-mid-infrared-instrument/miri-observing-modes/miri-medium-resolution-spectroscopy>).

applied, we take the weighted mean of the dithers to obtain the final spectrum for a filter/grating combination. The error of the spectrum is the propagated error of the weighted average.

As discussed previously, the flux calibration of the spectral cubes is not optimized due to the use of ground-based calibration files in the standard JWST pipeline. To produce a final flux-calibrated spectrum for VHS 1256 b, the extracted spectra must be multiplied by a scale factor, which is the ratio of a calibrated standard spectrum and the response it produces after processing with the JWST pipeline. The A3V star TYC 4433-1800-1, observed during commissioning (Program ID: 1128), has a calibrated flux reference in the CALSPEC Library (Bohlin et al. 2020) and was used as a calibrator to adjust the spectral response of the VHS 1256 b extracted spectrum.

All observation modes used in the ERS program were available for the calibrator star, and we reduced these observations with the same JWST pipeline parameters as the science spectra. As before, each dither was reduced individually, and the extracted spectra of each filter/grating mode were combined with a weighted mean to produce a final spectrum for that mode. There are oscillating features present in both the calibrator star and the VHS 1256 b NIRSpec spectra that are dependent on dither position and brightness. These features are averaged out in the calibrator star by fitting a fourth-order ($\sim T^4$) polynomial to obtain the “mean” response at each wavelength. The intrinsic spectral shape of the planetary-mass companion is not assumed, and the oscillations are not removed by fitting. The oscillating features change the amplitude of the extracted science spectra by about 2%–6%; however, in the extracted calibrator spectra these amplitudes can vary by as much as 20%, making the fitting step much more important for the calibrator star. In the VHS 1256 b–extracted spectra, the oscillations are visually apparent in dithers from the G140H/F100LP detector 1, G140H/F100LP detector 2, G140H/F100LP detector 1, and G140H/F100LP detector 2 observations. Averaging or taking the mean of several dithers helps to remove some of these oscillating features, but there are not enough dithers to remove the effect entirely. The calibrator star has oscillations in all observation modes for our program.

Portions of the final VHS 1256 b spectra that appear to be affected by these oscillations are 1.65–1.75 μm and 2–2.4 μm . We will discuss this in the context of identified molecular features in Section 4. Generally speaking, the crest-to-crest width of the oscillations appearing in the calibrator star extracted spectra vary in width, but are never smaller than .01 μm and can be as large as .029 μm .

The standard spectrum of our calibrator star possesses absorption features that are masked before fitting a fourth-order polynomial to the spectra. We perform each fit for a single filter/grating mode. The best fit of the calibrator spectrum and the best fit of the extracted pipeline spectra are divided to find the scale factor, which is then applied to the VHS 1256 b spectrum that falls within that bandpass. The extracted errors from the calibrator spectra are also included with VHS 1256 b’s spectrum errors when the scale factor is applied.

3.2. JWST/MIRI

Version 1.8.1 of the standard JWST pipeline was used to reduce the MIRI MRS observation listed in Table 1. The CRDS versions and context used by the JWST pipeline were “11.16.14” and “jwst_1007.pmap.” Each dithering sequence within a wavelength bandpass was combined to create a single spectral cube. JWST pipeline stages 1, 2, and 3 were all used to reduce the MIRI MRS data. The MIRI MRS dithers were reduced together for each channel/grating combination, and one-dimensional spectra were extracted from the resulting spectral cubes using aperture photometry.

We chose not to use the background subtraction method implemented in the standard pipeline, as it was unable to account for cosmic-ray showers present in the data. These cosmic-ray showers appear as diffuse, extended structures that do not produce the usual jumps in the detector ramps, which the pipeline is able to detect. The distribution and shape of the cosmic-ray showers vary between science and background exposures, and the impact of these differences produces the main systematic noise source for the faint point source extracted with MIRI. We instead estimated the background

Table 2
MIRI Background Observations

Instrument	Mode	Wavelength	Subarray	Readout	Resolving Power	Exposure Time (s)
MIRI	Channel 1, Short A	4.9–5.74	FULL	FASTR1	3320–3710	394.06
MIRI	Channel 1, Medium B	5.65–6.63	FULL	FASTR1	3190–3750	394.06
MIRI	Channel 1, Long C	6.53–7.65	FULL	FASTR1	3100–3610	394.06
MIRI	Channel 2, Short A	7.51–8.76	FULL	FASTR1	2990–3110	394.06
MIRI	Channel 2, Medium B	8.67–10.15	FULL	FASTR1	2750–3170	394.06
MIRI	Channel 2, Long C	10.01–11.71	FULL	FASTR1	2860–3300	394.06
MIRI	Channel 3, Short A	11.55–13.47	FULL	FASTR1	2530–2880	394.06
MIRI	Channel 3, Medium B	13.29–15.52	FULL	FASTR1	1790–2640	394.06
MIRI	Channel 3, Long C	15.41–18.02	FULL	FASTR1	1980–2790	394.06
MIRI	Channel 4, Short A	17.71–20.94	FULL	FASTR1	1460–1930	394.06
MIRI	Channel 4, Medium B	20.69–24.44	FULL	FASTR1	1680–1770	394.06
MIRI	Channel 4, Long C	23.22–28.1	FULL	FASTR1	1630–1330	394.06

Notes. Background observations taken with MIRI. The background observations were not used to reduce the VHS 1256 b spectra but are included in the summary of program observations. Resolution values for each of the instrument modes are from the following websites: MIRI (<https://jwst-docs.stsci.edu/jwst-mid-infrared-instrument/miri-observing-modes/miri-medium-resolution-spectroscopy>).

using a reference aperture placed off of the target in our calibrated science cubes. The separation of the background apertures varied between channels, with $1''.7$ for Channel 1, $2''.2$ for Channel 2, and $2''.3$ for Channels 3 and 4.

Before performing aperture photometry, as with NIRSpec, each spectral cube is collapsed in the wavelength direction using the mean, and the source center is fit with a 2D Gaussian. This is a necessary step due to slight band-to-band offsets still present in the distortion model of the MRS. We then extracted a flux within a circular aperture centered on our derived source position for each image along the spectral cube wavelength axis. For a given wavelength-dependent extraction radius (2.0 FWHM), the aperture correction is applied to account for the flux of the PSF missed outside of the extraction radius. This correction factor was derived using webbPSF (Perrin et al. 2014) models for the MRS, matching the empirical PSF FWHM measured during commissioning.

After extraction and aperture correction, fringes remain in portions of the MIRI spectrum. Fringing appears as a regular, beating interference pattern in the MIRI spectra (Argyriou et al. 2020), particularly in channels 2C, 3A, 3B, and 3C. The `ResidualFringeStep` is applied to the one-dimensional spectra to find and remove fringing patterns from the data (P. Kavanagh et al. 2023, in preparation).⁸¹

Past $18\ \mu\text{m}$, the sensitivity of the MRS drops significantly due to a combination of the low efficiency of the grating, low quantum efficiency of the detectors, and rising thermal background (Glasse et al. 2015). As a result, the spectrum could not reliably be extracted in channel 4. Instead, the cube was collapsed from 17.71 to $20.94\ \mu\text{m}$ (Channel 4A) to produce a single photometric point. The source center is found by fitting a 2D Gaussian to the collapsed channel 4A cube. A circular aperture (radius of 1.5 FWHM) is placed at the measured PSF center, and the same aperture correction described above is used. We measure the background using an off-target reference aperture with the same radius and subtract the background.

The error in the extracted spectrum was estimated using the propagated error by the `jwst` pipeline `Extract1dStep`.

⁸¹ This step is not automatically applied to the 1D spectra by the JWST pipeline at the moment. For more information, see <https://jwst-docs.stsci.edu/jwst-calibration-pipeline-caveats/jwst-miri-mrs-pipeline-caveats>.

The output `x1d.fits` files contain an `ERR` array extension that captures the error of the full processing chain, including the photon noise of the source. The extracted spectrum of the pipeline uses an annulus subtraction that introduces systematic errors from the background subtraction, but the overall spectrum matches the flux and shape of our own extraction. We therefore assume that the error reported by the pipeline should be representative of our own extraction. Indeed, the slope of the error follows the expected rising thermal background but seems to be overall a factor of ten lower than what one would expect from the ETC. Additionally, comparing with the noise from a collection of reference apertures around the field of view confirms this discrepancy. We therefore choose to artificially amplify the pipeline estimated error by a factor of 10, yielding a rather conservative estimate of the signal-to-noise ratio (S/N) until the pipeline issue is resolved.

The full reduced spectrum with labeled bandpasses is shown in Figure 2. The NIRSpec ($1\text{--}5\ \mu\text{m}$) spectra have an S/N of 50–400 per pixel. The MIRI ($4.9\text{--}20.94\ \mu\text{m}$) spectra have an S/N of 7 to 20 per pixel, with hardly any signal in Channel 4 ($17.66\text{--}28.1\ \mu\text{m}$). The photometry point from the channel has an S/N of 2.7.

3.3. NIRSpec–MIRI Instrument Overlap

There are 557 data points from NIRSpec and 370 data points from MIRI that overlap in wavelength. When the NIRSpec data are binned down and interpolated onto MIRI’s wavelength spacing, some portions of the NIRSpec data have a higher baseline flux, more than 3σ away from the MIRI data points. Figure 3 shows the overlap region of NIRSpec IFU and MIRI MRS data at the resolution of each respective instrument.

4. Atmospheric Features

This spectrum is one of the highest-S/N and broadest spectral coverage dataset of a brown dwarf or planetary-mass companion to date. With a spectral resolution of up to ~ 3000 , a wealth of atmospheric molecular features are revealed. In this section, we visually identify absorption features in the spectra and in some cases compare them to molecular cross sections. In each subsection, we discuss the molecules found and how they compare to similar brown dwarfs. The full VHS 1256 b spectrum displays several absorption features from atmospheric

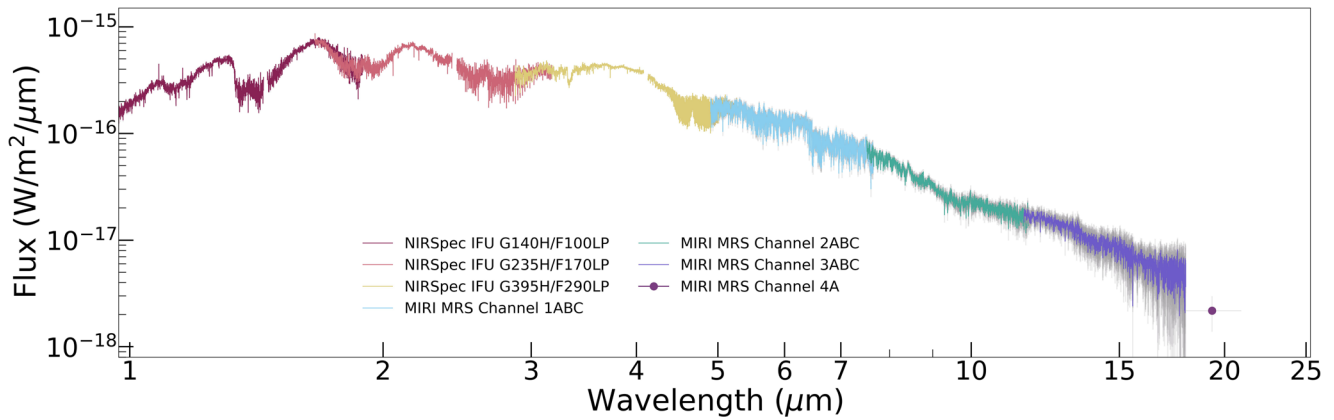


Figure 2. The full spectrum of VHS 1256 b using JWST’s NIRSpec IFU and MIRI MRS observation modes. Bandpasses are highlighted in different colors, and error bars are displayed in gray. A single photometric point for MIRI MRS Channel 4A is shown because there is little to no signal in the MIRI MRS 4B and 4C channels. Error bars are plotted in light gray. Reduced spectra are behind the figure but also hosted online.⁸²

gases that have been previously observed in brown dwarf and extended mid-infrared coverage that can constrain methane, water, and carbon monoxide. There is evidence for carbon dioxide as well. Across the spectrum, there are at least six detection regions of water, one visible methane feature, and two detections of carbon monoxide, which probe different pressure levels along the object’s pressure–temperature profile. From 8 to 12 μm , the spectral slope shows evidence of a silicate cloud. These atomic, molecular, and cloud features are highlighted in Figures 4 and 5.

4.1. Near-infrared Alkali Lines

Late M-dwarf stars and L spectral-type brown dwarfs display absorption features from neutral gases such as vanadium oxide (VO), iron hydride (FeH), potassium (K), titanium oxide (TiO), and sodium (Na). These absorption features can be used to infer surface gravity. Broader and deeper absorption features from these molecules and atoms correspond to higher surface gravity and older ages (McGovern et al. 2004; Allers & Liu 2013). The 1 to 1.35 μm portion of the JWST/NIRSpec spectrum (top, Figure 4) holds two K doublets and a Na line that indicate a relatively low surface gravity, which is consistent with VHS 1256 b’s placement on a color–magnitude diagram. Figure 6 shows a comparison of VHS 1256 b’s Na and K lines with those of field brown dwarfs. Both absorption lines appear narrower than the same lines in a similar spectral-type field brown dwarf, indicating a low surface gravity for VHS 1256 b. The first published near-infrared spectrum of VHS 1256 b in Gauza et al. (2015) showed no K doublet features and no detection of the 1.134 μm Na line, possibly due to insufficient resolution. Follow-up work by Petrus et al. (2023) obtained medium-resolution ($R \sim 8000$) spectra of VHS 1256 b at a resolution higher than the JWST spectrum presented here. The Na line at 1.134 μm and K doublets at 1.173 and 1.248 μm are easier to distinguish from the continuum in the JWST spectrum; however, the published spectrum from Petrus et al. (2023) likely has the resolution to capture a broader range of absorption features such as Fe, FeH, and TiO. However, the standard NIRSpec pipeline procedures are still in development. Once these parameters have been refined, future reductions of

the JWST spectrum may lead to the detection of finer features with higher S/Ns.

4.2. Water

All spectral types of brown dwarfs possess absorption features due to water vapor in the near and mid-infrared. The shape and depth of these features are primarily determined by the effective temperature or spectral type of a brown dwarf (Allers & Liu 2013). Previously published space-based spectroscopic infrared observations of VHS 1256 b and other brown dwarfs are sensitive to water but often limited to resolutions of a few hundred (Zhou et al. 2020). The sensitivity and added resolution of the JWST data provide crucial details regarding the presence of water vapor in the atmospheres of brown dwarfs. Water absorption bands are present in the VHS 1256 b spectrum at 1.3–1.6 and 1.7–2.1 μm , and shape the spectrum beyond 10 μm . Water overlaps with carbon monoxide (CO) between 2.2 and 2.6 μm and between 4.3 and 5 μm . All water features are labeled in Figures 4 and 5.

4.3. Methane

Brown dwarfs below an effective temperature of ~ 1400 K begin to display methane absorption features, as methane is favored in the chemical reaction between methane and carbon monoxide at these temperatures (Lodders & Fegley 2002). Methane absorption at 1.67 μm is also a typical T-dwarf signature (Cushing et al. 2005).

We have an absorption feature in the spectrum at 1.66 μm in VHS 1256 b; however, this feature is slightly blueward of the typical 1.67 μm location, but also too broad to be FeH absorption that is seen in warmer L dwarfs (Cushing et al. 2005). This feature also coincides with excess amplitudes from oscillations in the extracted dithers at wavelengths between 1.65 and 1.75 μm . Only dithers 2 and 3 of the total four show no oscillations in the extracted spectra, but the slight depression remains when only using dithers 2 and 3 of the observations. The crest-to-crest width of the oscillation waves in the calibrator star between 1.65 and 1.75 is ~ 0.01 – 0.02 μm , and the width of the potential methane feature is 0.02 μm . Previously published near-infrared spectra show no methane absorption at 1.67 μm (Gauza et al. 2015; Petrus et al. 2023). If this feature remains after further pipeline updates, the opacity

⁸² https://github.com/bemiles/JWST_VHS1256b_Reduction/tree/main/reduced_spectra

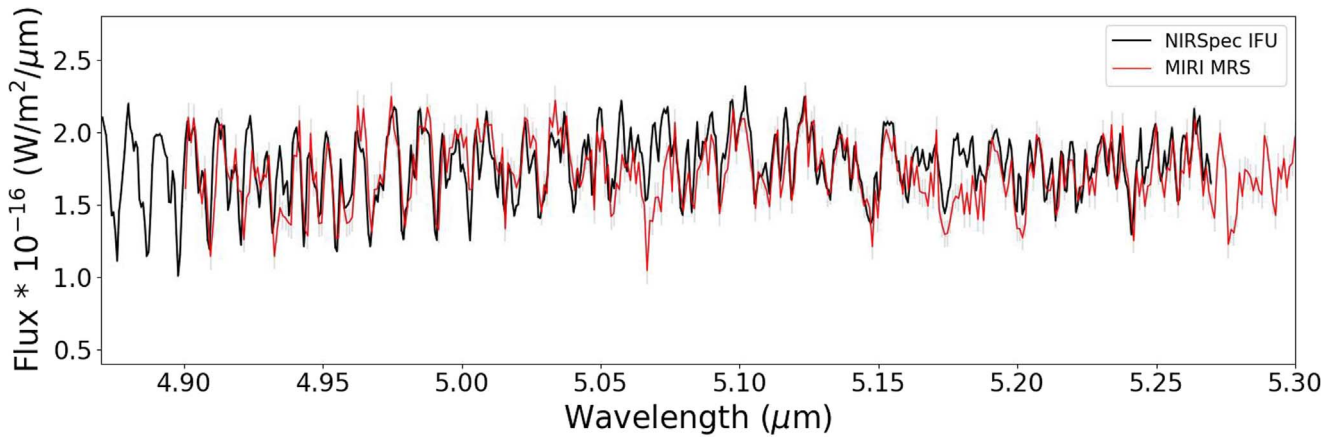


Figure 3. The wavelength overlap region between JWST’s NIRSpec IFU (black) and MIRI MRS (red) observation modes with errors plotted in light gray. The flux-calibrated NIRSpec IFU spectra agree well with the MIRI MRS extracted spectra in the overlap region.

source causing this feature will need to be validated with further atmospheric modeling work.

We also find a relatively shallow methane feature between 2.8 and 3.8 μm that is consistent with the previously published *L*-band spectrum in Miles et al. (2018). Methane absorption at $\sim 3.3 \mu\text{m}$ is more prominent in brown dwarfs than methane absorption at 1.65 μm and is seen even in mid-*L* dwarfs (Noll et al. 2000). In this effective temperature range, methane has a significant opacity contribution between 7 and 9 μm , but its overall strength compared to water and other molecules is smaller. This region does not visually mirror the predicted opacity profile of methane for this reason.

All of the near-infrared and mid-infrared methane features appear depleted relative to similar-temperature brown dwarfs, indicating that disequilibrium chemistry is influencing the apparent abundance of methane in the upper atmosphere. We will discuss the degree of atmospheric mixing required to recreate these methane features with models in Section 5.

4.4. Carbon Monoxide

Carbon monoxide (CO) is a common near-infrared spectral feature in very low-mass stars and brown dwarfs with effective temperatures above ~ 1400 K (Lodders & Fegley 2002; Cushing et al. 2005). Carbon monoxide produces a strong feature centered at 4.6 μm in warm brown dwarfs. Cooler brown dwarfs that have disequilibrium chemistry driven by atmospheric mixing (Sorahana & Yamamura 2012) also display this feature. VHS 1256 b’s effective temperature is cool enough that a small degree of carbon monoxide will be detected at 2.3 μm . The depth and shape of the central feature are similar to previously published K-band spectra in Hoch et al. (2022) and Petrus et al. (2023). We also detect a densely packed set of carbon monoxide features around 4.6 μm in VHS 1256 b’s spectrum. It is the best-resolved, highest-S/N set of features from the fundamental carbon monoxide bandhead compared to previously published space-based brown dwarf spectra and photometry from AKARI (Sorahana & Yamamura 2012) and Spitzer (Patten et al. 2006).

4.5. Carbon Dioxide

Carbon dioxide (CO_2) is another carbon- and oxygen-bearing gas that can provide insight into metallicity or atmospheric effective temperature (Lodders & Fegley 2002; Tsuji et al. 2011; Sorahana & Yamamura 2012). The CO_2

feature at 4.2 μm is inaccessible from ground-based observatories and has only been detected in a handful of mid-infrared observations of T-type brown dwarfs (Tsuji et al. 2011; Sorahana & Yamamura 2012). We show evidence for this CO_2 feature in the JWST spectrum of VHS 1256 b by comparing two versions of an atmospheric model, one with CO_2 opacities added and one without, as shown in Figure 7. The model comparisons reveal a slight absorption feature where CO_2 influences the spectrum from 4.2 to 4.4 μm . In M dwarfs and relatively warm L dwarfs, CO_2 is theorized to primarily trend with effective temperature, while at lower effective temperatures where methane should be the dominant carbon-bearing gas, CO_2 will vary with both atmospheric pressure and temperature (Lodders & Fegley 2002). The presence of CO_2 in VHS 1256 b’s spectrum would not be surprising, but it needs to be verified with more detailed atmospheric analysis.

4.6. Clouds

The transition between red to blue near-infrared colors at the L-to-T transition shown in Figure 1 is likely driven by the condensation and eventual descent below the photosphere of silicate grains composed of enstatite, forsterite, or quartz as these objects cool. Low-surface-gravity brown dwarfs and directly imaged exoplanets can retain their silicate clouds at lower effective temperatures, producing their redder colors compared to field counterparts. VHS 1256 b displays a significant silicate cloud feature in the JWST/MIRI spectrum from 8 to 11 μm when compared to a standard brown dwarf and the relatively red brown dwarf 2MASSW J2224438–015852 (2M2224–0158) discovered in Kirkpatrick et al. (2000), which is an outlier along the L-to-T transition (Figure 11). Compared to 2M2224–0158, VHS 1256 b shares the same spectral shape across 8–11 μm , indicating an absorption feature due to silicate clouds of similar composition. The best-fit cloud model for 2MASS 2224–0158 from Burningham et al. (2021) was a combination of enstatite (MgSiO_3), quartz (SiO_2), and a higher-pressure iron (Fe) cloud.

4.7. Other Molecular Gases and Clouds

VHS 1256 b’s spectrum shows evidence of disequilibrium chemistry based on methane and carbon monoxide; therefore, we explored the potential presence of other disequilibrium molecules.

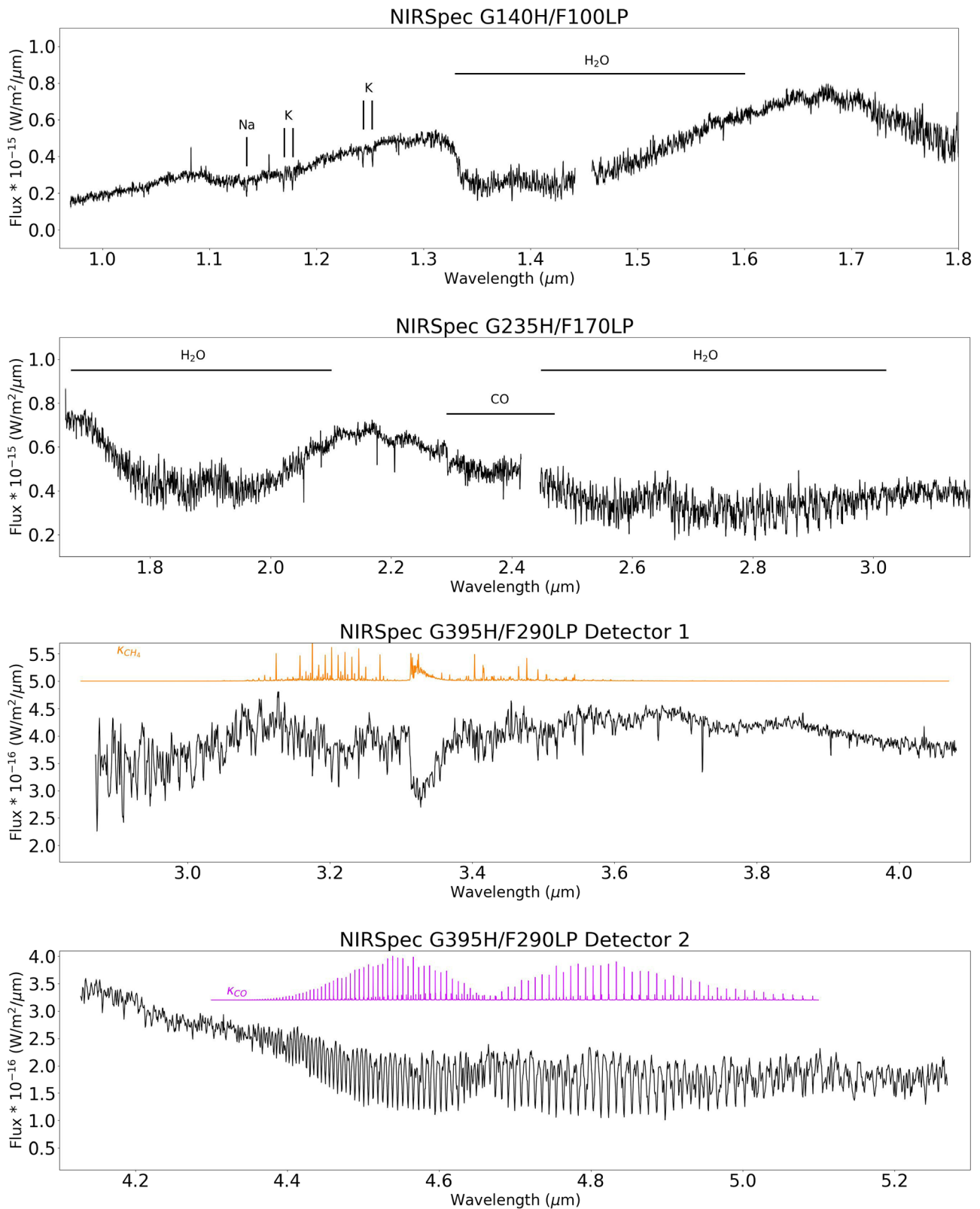


Figure 4. JWST/NIRSpec spectrum of VHS 1256 b, with important molecular gases highlighted. Molecules were identified via visual comparison with template spectra.

From the equilibrium Sonora Bobcat models (Marley et al. 2021), we scaled different molecular abundances to search for species that could appear in disequilibrium conditions. In VHS 1256 b's spectrum, there are no obvious signs of acetylene (C_2H_2), ethylene (C_2H_4), ethane (C_2H_6), hydrogen sulfide

(H_2S), phosphine (PH_3), or hydrogen cyanide (HCN). Outside of the features listed prior to this subsection, more detailed analysis and approaches such as retrievals and cross-correlation will need to be applied to the JWST VHS 1256 b spectra to fully understand the object's atmospheric chemistry.

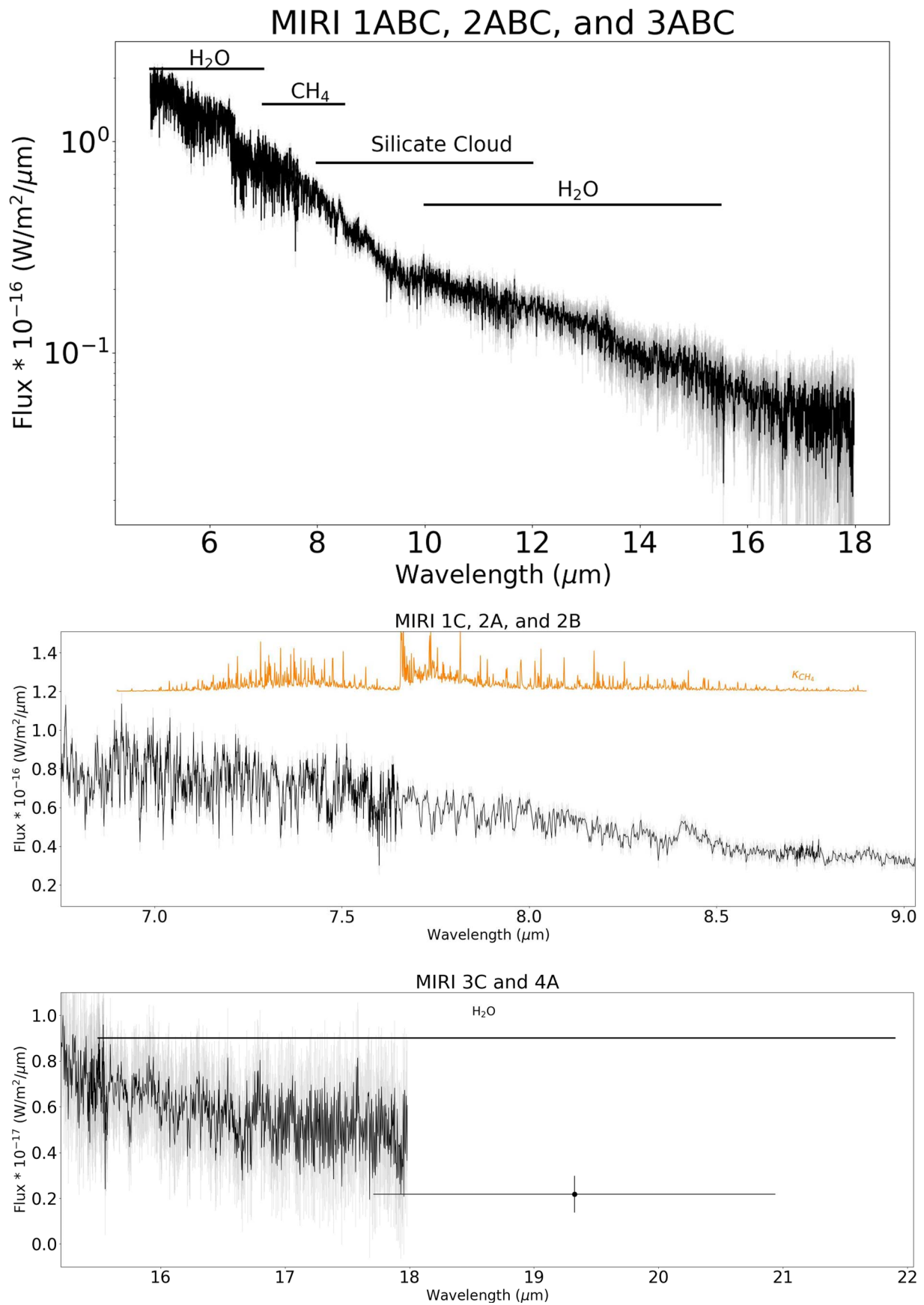


Figure 5. JWST/MIRI spectrum of VHS 1256 b, with important molecular gases highlighted. Molecules were identified via visual comparison with template spectra.

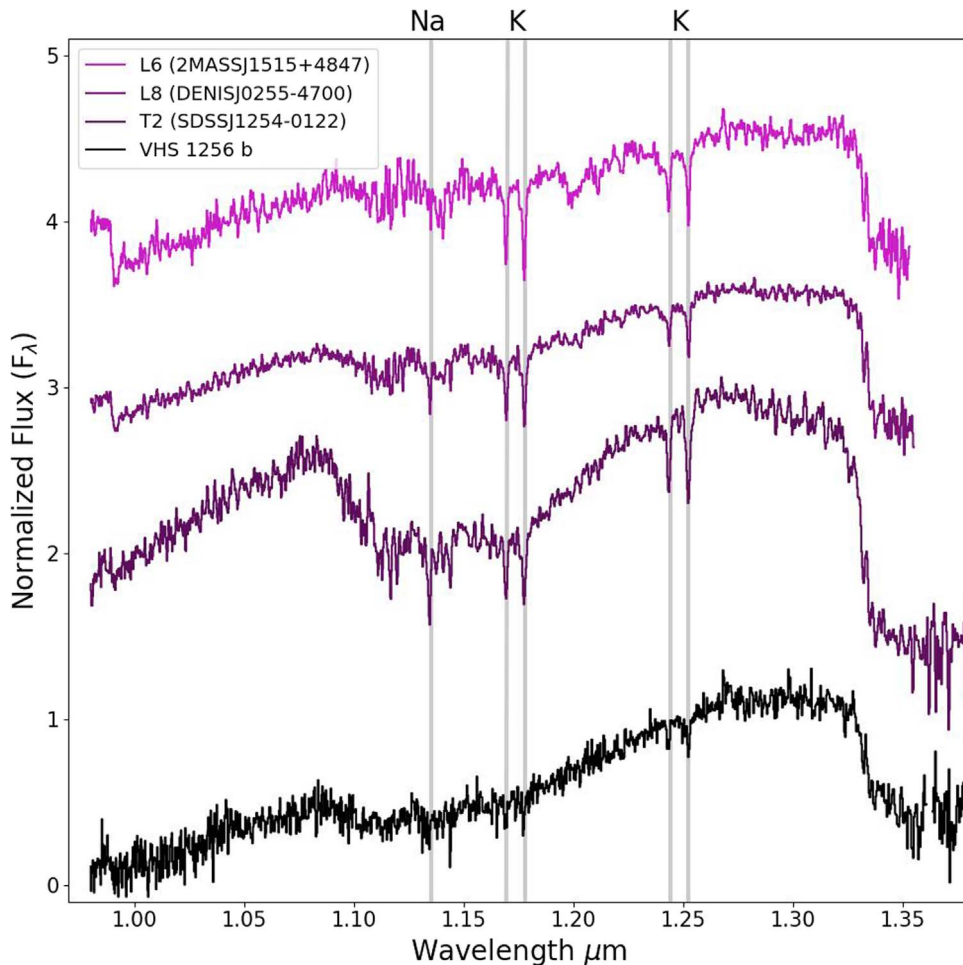


Figure 6. Template brown dwarf spectra from Allers & Liu (2013) (colored) compared to VHS 1256 b (black). Field brown dwarfs that possess high surface gravities display broader Na and K lines than VHS 1256 b, implying the low surface gravity of VHS 1256 b.

5. Atmospheric Modeling

We used the long-developed EGP substellar code (Marley et al. 1996; Fortney et al. 2005, 2007, 2008; Marley et al. 2012; Morley et al. 2014; Marley et al. 2021; Karalidi et al. 2021; Mukherjee et al. 2023) to find the best-fit forward model for the observed JWST spectrum. This lineage of codes parameterizes the cloudiness of an object using the sedimentation parameter f_{sed} and parameterizes the mixing strength using the eddy diffusion coefficient K_{zz} (Ackerman & Marley 2001). A higher value of f_{sed} describes less optically thick clouds with larger particles: lower values produce thicker clouds with smaller particles. The eddy diffusion coefficient K_{zz} has higher values if atmospheric mixing is strong, potentially driving the atmosphere out of chemical equilibrium (Saumon et al. 2006; Hubeny & Burrows 2007) and also extending the extent of atmospheric cloud decks. The goal of our atmospheric modeling efforts is to capture the prominent atmospheric physics and chemistry that influences the spectrum of VHS 1256 b, and the EGP family of codes is well-suited to this task, although modeling VHS 1256 b’s full spectrum required careful fine-tuning of parameters to capture the object’s disequilibrium chemistry and cloudiness.

We used PICASO 3.0 (Mukherjee et al. 2023), a modified Python version of the Fortran-based EGP code that includes the capability of self-consistently modeling both disequilibrium chemistry and clouds simultaneously with a pressure-

dependent K_{zz} profile. The details of the code are described in Mukherjee et al. (2023), and the opacity sources used are detailed in Table 3 in Mukherjee et al. (2023). We first explored a small grid with temperatures running from 900 K to 1600 K at intervals of 100 K and f_{sed} values of 1, 2, 3, and 8. Each atmospheric model has 90 layers spaced in atmospheric pressure. The spectra were post-processed to mirror the abundances of an atmosphere with two different uniform K_{zz} profile values, $10^5 \text{ cm}^2 \text{ s}^{-1}$ and $10^8 \text{ cm}^2 \text{ s}^{-1}$. The smaller value of K_{zz} corresponds to the theoretically estimated K_{zz} (Zahnle & Marley 2014) value, and the higher value matches previously published mixing values estimated from the $3 \mu\text{m}$ methane feature in Miles et al. (2018). The best attempt at a fine-tuned model that matches the overall shape of the spectrum had parameters $T_{\text{eff}} = 1100 \text{ K}$, $f_{\text{sed}} = 1$, $\log(g) = 4.5$, and $K_{zz} = 10^8 \text{ cm}^2 \text{ s}^{-1}$. However, the best-fit model from this initial grid produced too much flux in the near-infrared despite matching the majority of the molecular absorption features. The estimated temperature is similar to effective temperatures ($1122 \pm 16 \text{ K}$ and $1171 \pm 17 \text{ K}$), derived in Dupuy et al. (2022) using atmospheric evolution models from Saumon & Marley (2008). Our forward-modeling approach produces lower effective temperatures compared to the forward-model-derived effective temperatures in Hoch et al. (2022) (1200 K) and Petrus et al. (2023) (1380 K) but higher than the temperature derived in Zhou et al. (2020) (1000 K).

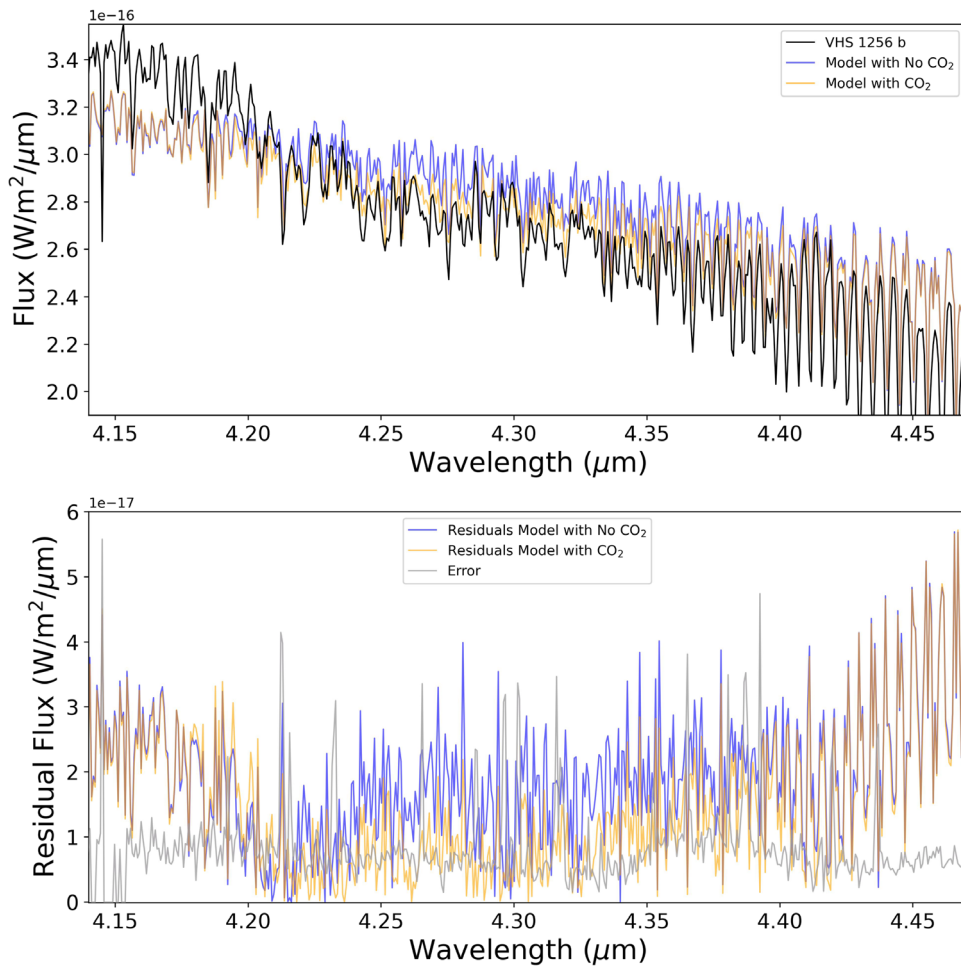


Figure 7. The JWST/NIRSpec spectrum of VHS 1256 b compared to two atmospheric models that contain CO₂ (orange) and a model with no opacity from CO₂ (blue). The data show excess absorption at 4.2 μm, which shows evidence of CO₂ absorption. The bottom panel shows residuals between the data and the models with the error plotted in gray. No CO₂ shows a larger residual than a model including the opacity of the molecule.

In order to better fit the observed near-infrared flux, we adopted a two-cloud model and added a self-consistent treatment of atmospheric mixing to estimate K_{zz} as a function of pressure. This modeling approach in PICASO 3.0 simultaneously includes the heating/cooling due to clouds and mixing-induced disequilibrium chemistry while calculating the atmospheric structure of the object. Instead of a single cloud with an f_{sed} of 1, we used a mixture of two clouds, with 90% of the modeled clouds having $f_{\text{sed}} = 0.6$ and 10% of the modeled clouds having $f_{\text{sed}} = 1.0$. The clouds described by the lower $f_{\text{sed}} = 0.6$ value produce a thicker, deeper cloud layer that helps match the model to the observed spectral shape of VHS 1256 b. The fluxes for each of these cloudy disequilibrium chemistry models were first calculated separately and were then linearly combined using

$$F_{\text{total}} = fF_1 + (1 - f)F_2 \quad (1)$$

to obtain the total flux (F_{total}), which is shown in Figure 8. In Equation (1), f represents the fractional coverage of one of the cloudy models, F_1 , and F_2 represents the fluxes calculated from models with clouds with a particular f_{sed} . The use of two clouds is motivated by the object’s measured variability, which is caused by changes in the surface brightness potentially created by moving cloud patches. Using a self-consistent and pressure-

dependent approach to estimate atmospheric mixing, we find K_{zz} values ranging from $10^8 \text{ cm}^2 \text{ s}^{-1}$ to $10^9 \text{ cm}^2 \text{ s}^{-1}$ along the pressure–temperature profile. The best-fit spectrum using these parameters is shown in Figure 8, and the atmospheric profile and chemistry are described in Figure 9.

The best-fit atmospheric model matches the overall shape of the 1–20 μm spectrum of VHS 1256 b with discrepancies occurring where the silicate cloud feature appears and also around the peak from 1.5 to 1.8 μm, where the spectrum is shaped by water and collisionally induced absorption from hydrogen. The major equilibrium and disequilibrium absorption features described in Section 4 are not exactly matched and dampened because of atmospheric clouds. The chemical abundance profile of the best-fit model demonstrates that water and carbon monoxide are relatively insensitive to atmospheric mixing. The volume mixing ratios of methane, ammonia, and carbon dioxide are affected by atmospheric mixing; however, based on Section 4, only carbon dioxide and methane produce visible spectral features.

6. Discussion

6.1. Bolometric Luminosity and Mass

Integrating over VHS 1256 b’s JWST spectrum and using the best-fit model described in the previous section to estimate

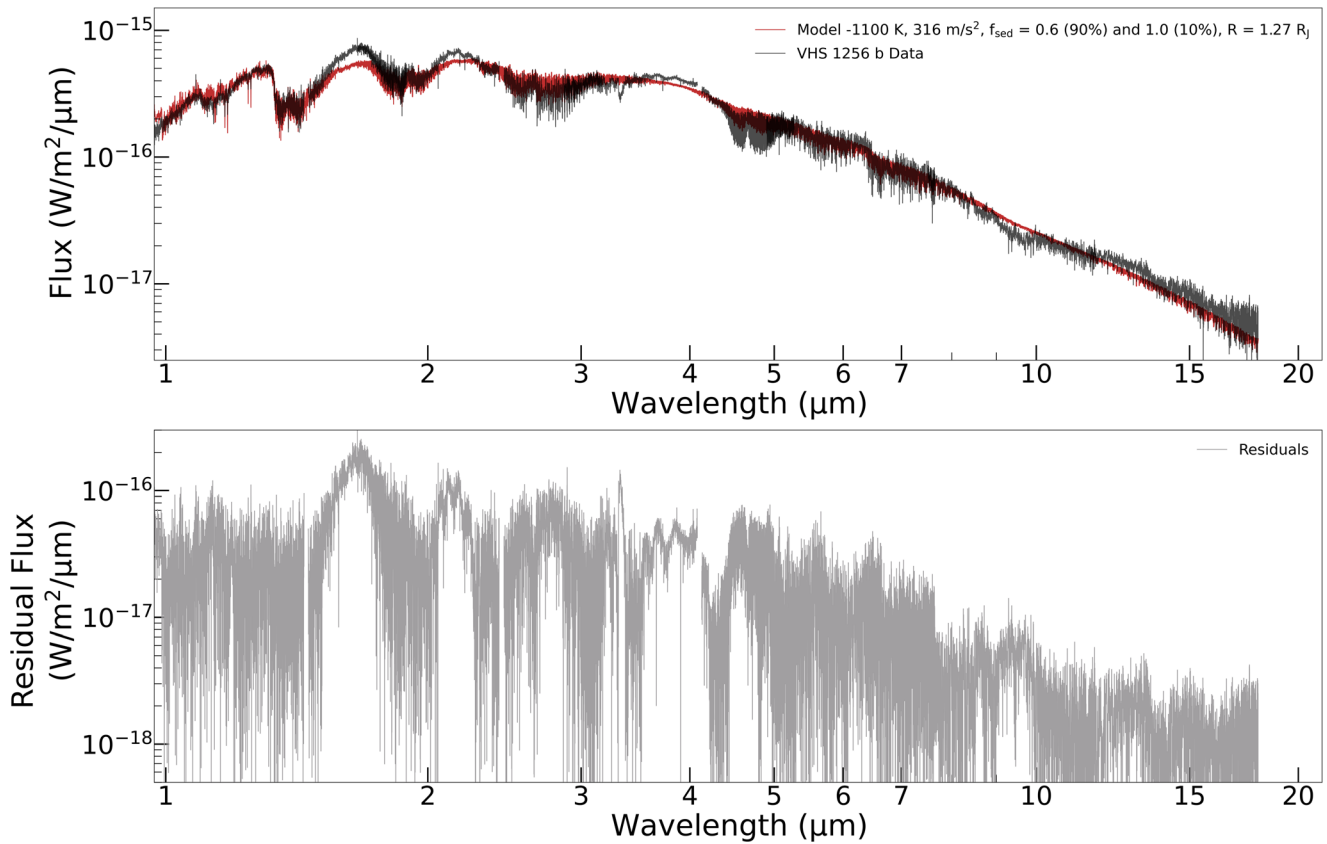


Figure 8. (Top panel) The best-fit model atmospheric model (red) compared to the VHS 1256 b spectrum (black). The residual fluxes between the best-attempt model and VHS 1256 b’s spectrum. The largest discrepancies are in the near-infrared and within absorption lines that are muted due to the model’s cloudiness.

(The data used to create this figure are available.)

flux from wavelength ranges not covered by our JWST spectrum, we find a bolometric luminosity of $\log\left(\frac{L_{\text{bol}}}{L_{\odot}}\right) = -4.55 \pm 0.009$, adopting the Gaia Early Data Release 3 distance measurement to the system of 21.15 ± 0.22 pc (Gaia Collaboration et al. 2021). Our JWST spectrum covers most of the full luminous range of VHS 1256 b; 98% of the measured luminosity is derived directly from the spectrum, with only 2% extrapolated from model fits to wavelengths outside of our JWST wavelength coverage. So much of the SED is covered by measurements and so many independent bands are included that the statistical/random error on our bolometric luminosity value is very small. With a precise distance measurement from Gaia Collaboration et al. (2021) for this system, the most significant uncertainty will stem from the absolute flux calibration of the spectrum using the A3V star TYC 4433-1800-1 (see Section 3). Over the course of JWST’s operation, a dedicated absolute flux calibration program is planned to enable better than 2% flux calibration over a wide range of objects (Gordon et al. 2022). Thus, to set the error on our bolometric luminosity measurement at the current early stage of the JWST mission, we estimate a conservative error on the absolute flux calibration of 3% and add this in quadrature with the error on the integrated spectrum.

Adopting the Gaia DR3 distance for the system, a spectral type of $L7 \pm 1.5$ and the VISTA Hemisphere survey K_S photometry from Gauza et al. (2015), and a bolometric correction BC_{K_S} based on the polynomial relationship for young M- to T-type objects from Filippazzo et al. (2015), we

find a photometric bolometric luminosity of $\log\left(\frac{L_{\text{bol}}}{L_{\odot}}\right) = -4.60 \pm 0.05$, in good agreement with the value derived from our JWST spectroscopy. However, recent bolometric luminosity estimates from ground-based, near-IR spectroscopy for VHS 1256 b are slightly fainter than the value we find with JWST: Hoch et al. (2022) find a best value of $\log\left(\frac{L_{\text{bol}}}{L_{\odot}}\right) = -4.67$, within the range from -4.6 to -4.7 , while Petrus et al. (2023) find $\log\left(\frac{L_{\text{bol}}}{L_{\odot}}\right) = -4.67 \pm 0.07$. The bolometric luminosity estimate from Petrus et al. (2023) adopts a distance of $22.2^{+1.1}_{-1.2}$ pc from Dupuy et al. (2020), rather than the more accurate Gaia eDR3 measurement. Adjusting to the Gaia distance measurement leads to a slightly smaller bolometric luminosity, further increasing the tension between the JWST measurement and ground-based spectroscopic measurements.

Dupuy et al. (2022) determine an updated age for the system of 140 ± 20 Myr from dynamical masses derived from orbital fits to the inner AB binary. VHS 1256 b sits close to the deuterium-burning limit—if VHS 1256 b is slightly above the deuterium-burning limit, it will be actively burning deuterium at this age. For the short duration of its deuterium-burning phase, a lower-mass object may be more luminous than a higher-mass object at the same age; see Figure 10. As a given luminosity can correspond to a range of masses in this case, direct interpolation from this model grid can produce erroneous mass estimates.

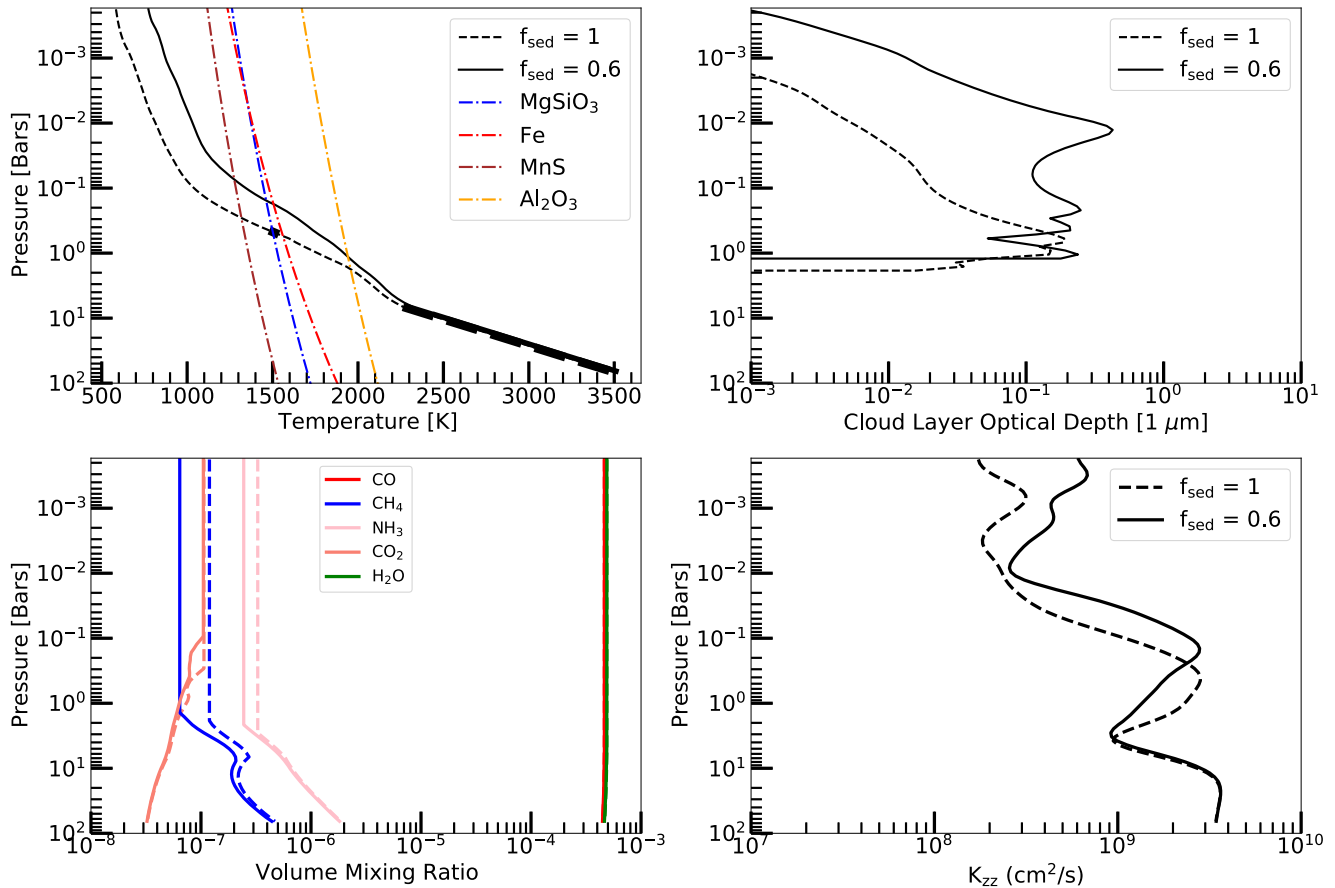


Figure 9. Atmospheric parameters of VHS 1256 b. Top left: the pressure–temperature profile (black) with convective regions highlighted with thicker black lines. The condensation curves of cloud opacities included within the model are shown as colored lines. Top right: the optical depth profile of the clouds used in the hybrid best-fit model. Lower f_{sed} values produce a higher opacity through a larger region of the atmosphere compare to higher f_{sed} values. Lower left: the abundance of different atmospheric molecules as a function of pressure. Atmospheric mixing influences abundances primarily below $\log(P) = 0$ bars. Lower right: atmospheric mixing, K_{zz} , as a function of pressure. Stronger mixing occurs at higher pressures.

To robustly estimate the mass of VHS 1256 b, we implemented a rejection-sampling method similar to that described in Dupuy et al. (2022). First, we draw 1×10^6 samples of age and mass from a Gaussian distribution in age around 140 Myr, with $\sigma = 20$ Myr, and a uniform distribution in mass from 1 to $50 M_{\text{Jup}}$. For each age and mass sample, we then interpolate a model luminosity from an evolutionary model grid and calculate χ^2 as $\chi^2 = \frac{(L_{\text{bol,model}} - L_{\text{bol,measured}})^2}{\sigma_{L_{\text{bol,measured}}}^2}$, then convert to a probability (P) by normalizing by the minimum χ^2 ($P = e^{-\frac{\chi^2 - \chi_{\text{min}}^2}{2}}$) value among our 1×10^6 samples. For each sample, we also draw a uniformly distributed number from 0 to 1. We retain the samples where the sample probability is greater than the uniformly distributed variate drawn for that sample.

As VHS 1256 b has strong evidence for the presence of clouds in its spectrum from the detection of the silicate feature at $10 \mu\text{m}$, we implemented this rejection-sampling procedure using the hybrid cloud grid of Saumon & Marley (2008), which includes clouds for objects with L-type spectra and clear atmospheres for objects with T-type spectra.

A histogram of the final set of accepted masses is shown in Figure 10. We find a bimodal distribution of masses, with accepted samples both above and below the deuterium mass-burning limit, as also seen in Dupuy et al. (2022). The percentage of samples that fall into each of the two peaks depends strongly on both the bolometric luminosity value and

the uncertainty on that value. While we cannot conclusively determine whether VHS 1256 b falls above or below the deuterium mass-burning limit, all accepted samples for this model have masses $< 20 M_{\text{Jup}}$.

6.2. Variability

Young, planetary-mass objects with mid-to-late-L spectral types are highly variable in the near-IR (Biller et al. 2015; Lew et al. 2016; Biller et al. 2018; Zhou et al. 2020; Bowler et al. 2020), with variability amplitudes $> 5\%$ over observations a few hours in length. VHS 1256 b is the most variable of this cohort. Over a contiguous six-orbit observation with HST/WFC3 obtained in 2018, Bowler et al. (2020) found that VHS 1256 b varied by $> 20\%$ between 1.1 and $1.7 \mu\text{m}$ over 8 hr. In the near-IR, Bowler et al. (2020) fit the observed HST trend with a single sinusoidal model; however, in an additional 15 orbit/42 hr HST/WFC3 observation in 2020 presented by Zhou et al. (submitted), the variability observed is more complex, requiring a three-sinusoid + slope model for a full fit. In the mid-IR, Zhou et al. (2020) obtained a contiguous 36 hr Spitzer $4.5 \mu\text{m}$ lightcurve of VHS 1256 b and found a best-fit model for this lightcurve of a single sinusoid with a period of 22.04 ± 0.05 hr (interpreted as the rotation period of the object) and a peak-to-peak amplitude of $5.76\% \pm 0.04\%$, a significantly lower variability amplitude when compared to the near-IR variability. Both the near-IR and mid-IR variability are

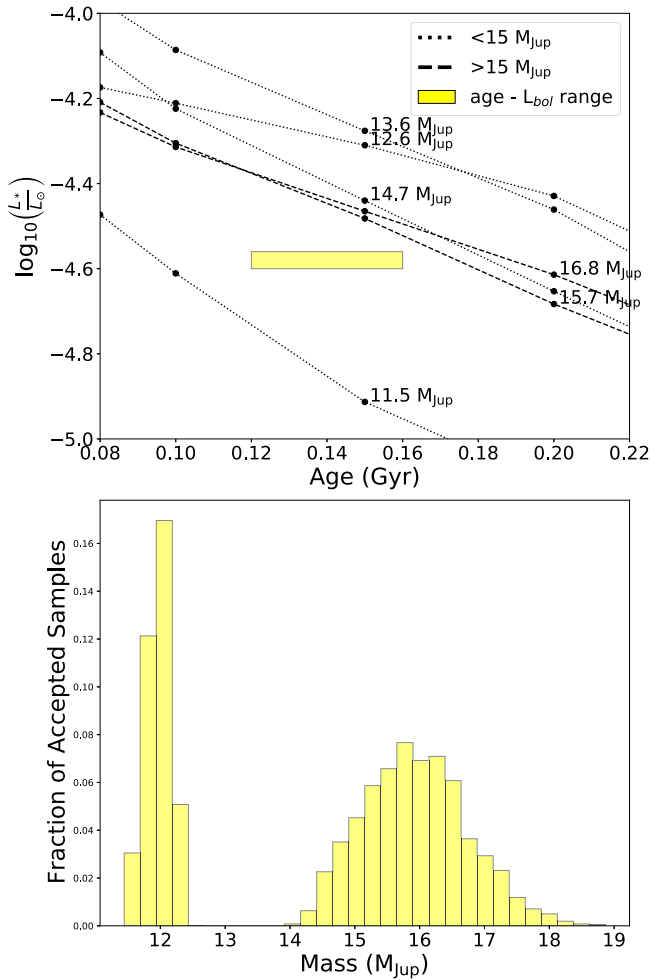


Figure 10. Top: mass vs. luminosity tracks from the hybrid cloud grid from Saumon & Marley (2008). Models for masses $< 15 M_{\text{Jup}}$ are shown as dotted lines; models for masses $> 15 M_{\text{Jup}}$ are shown as dashed lines. The expected age–bolometric luminosity range of VHS 1256 b is shown by the yellow rectangle. At the ages considered here, lower-mass objects burning deuterium may have higher luminosities than higher-mass objects that have already completed deuterium burning. Bottom: histograms of the final sets of accepted masses drawn from the same grid. The distribution is bimodal, with peaks both above and below the deuterium mass-burning limit. While we cannot conclusively determine whether VHS 1256 b lies above or below the deuterium mass-burning limit, all accepted samples had masses $< 20 M_{\text{Jup}}$.

likely driven by patchy thin and thick silicate clouds (Apai et al. 2013). Variability is an important probe of the inhomogeneity of the top-of-atmosphere structure of these objects and it is critical to understand the intrinsic variability of this target in order to interpret our JWST observations. To do so, we have conducted a multitelescope, multiepoch photometric variability monitoring campaign starting in 2022 February and continuing through July, directly covering the JWST observation epoch, which will be presented in B. A. Biller et al. (in preparation).

However, over the ~ 4 hr timescale of our ERS observations, we expect a relatively low level of variability, based on estimates from the earlier HST and Spitzer observations. To estimate the range of potential variability we expect during the NIRSpec observation, we drew 10,000 sample 2 hr observations from the three-sinusoid model from Zhou et al. (2022) and estimated the intrinsic variability occurring during each simulated observation as the maximum minus the minimum

value from the model during that time span. We used a very fine time sampling and did not realistically simulate noise or the actual cadence of our JWST observations. Thus, this method constrains the intrinsic variability, and the actual measurement of variability in any given observation would yield a smaller value than these predictions. From our simulated observations, 50% of samples varied by less than 1.5%, 75% of samples varied by less than 2.5%, and 95% of samples varied by less than 3.7%. For wavelengths $> 3 \mu\text{m}$, drawing 10,000 sample 2 hr observations from the single-sinusoid model used to fit the Spitzer $4.5 \mu\text{m}$ lightcurve from Zhou et al. (2020), 50% of samples varied by less than 1.1%, 75% of samples varied by less than 1.5%, and 100% of samples varied by less than 1.6%. More conservatively, we estimate a maximum potential variability measurement of 5% over 2 hr for the JWST/NIRSpec $1\text{--}3 \mu\text{m}$ observations, based on the highest amplitude variability epoch, where VHS 1256 b displayed 20% variability over 8 hr (Bowler et al. 2020). Assuming the same scaling between near-IR and mid-IR lightcurves as found between the HST and Spitzer lightcurves of Bowler et al. (2020) and Zhou et al. (2020), we estimate a maximum potential variability measurement of 1.5% over 2 hr at wavelengths $> 3 \mu\text{m}$. Variability has not been measured beyond $5 \mu\text{m}$ for any planetary-mass object, but assuming a continuing trend of decreasing variability amplitude with increasing wavelength, we expect variability at wavelengths $> 5 \mu\text{m}$ to be negligible.

6.3. Atmospheric Chemistry

The JWST spectrum has molecular features that are consistent with previous findings of VHS 1256 b and other young, red late-L dwarfs having atmospheres that are out of chemical equilibrium (Chauvin et al. 2004; Gauza et al. 2015; Liu et al. 2016; Miles et al. 2018). The presence of CO absorption and depleted CH_4 absorption compared to equilibrium atmospheric models supports atmospheric mixing forcing the atmosphere into chemical disequilibrium. The CH_4 absorption feature at $3.3 \mu\text{m}$ is the most prominent absorption feature stemming from disequilibrium chemistry in VHS 1256 b’s spectrum and potentially other similar-temperature, directly imaged exoplanets. The fine-tuned forward model shown in Figure 8 has an associated CH_4 abundance profile (Figure 9), but the model does not match the $3.3 \mu\text{m}$ CH_4 feature or many other molecular features along the spectrum, despite matching the overall SED shape. For sedimentation parameter values of $f_{\text{sed}} = 4$, CH_4 features at 1.6 and $7 \mu\text{m}$ appear in model spectra, but for our best-fit model with $f_{\text{sed}} < 1$, these features are quite muted. The estimated K_{zz} range of VHS 1256 b spans $10^8 \text{cm}^2 \text{s}^{-1}$ – $10^9 \text{cm}^2 \text{s}^{-1}$, which is consistent with the estimated K_{zz} of $10^8 \text{cm}^2 \text{s}^{-1}$ from Miles et al. (2018). However, not matching crucial disequilibrium absorption features is significant and means future modeling work on clouds and mixing will need to be done to estimate a meaningful K_{zz} for VHS 1256 b.

We show evidence of CO_2 being useful for reproducing the shape of the JWST spectrum at $4.2 \mu\text{m}$ as shown in Figures 7 and 9. The portions of the JWST spectrum surrounding the CO_2 feature are discrepant from the best-fit atmospheric model. CO_2 is also influenced by disequilibrium chemistry, but the timescale of CO_2 ’s conversion from CH_4 is much faster than the conversion of CO to CH_4 (Zahnle & Marley 2014); therefore, CO_2 quenches at higher atmospheric pressures.

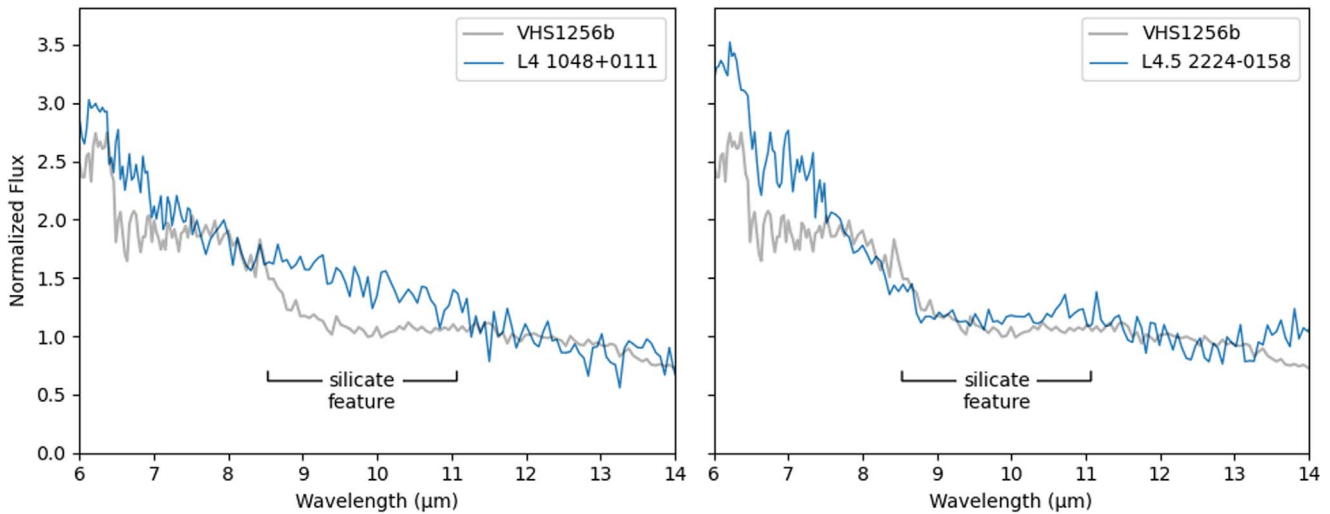


Figure 11. The JWST/MIRI spectrum of VHS 1256 b is a good match to the Spitzer spectrum of 2M2224–0158, which has a prominent silicate absorption feature. 2M1048+0111, which does not have a prominent silicate feature, is shown for comparison. (2M2224–0158 and 2M1048+0111 spectra from Suárez & Metchev 2022).

Historically, disequilibrium chemistry driven by atmospheric mixing has only been detectable from a single molecule in exoplanets and brown dwarfs: either CH_4 for warmer L dwarfs or CO for cooler T dwarfs. JWST has the capability to confidently detect two different molecular gases with different quench pressures between 1 and $5 \mu\text{m}$. JWST is capable of detecting CO_2 and CH_4 or CO over the entire L-, T-, and potentially Y-dwarf sequence, revolutionizing our understanding of disequilibrium chemistry as traced by carbon species in the atmospheres of brown dwarfs and extrasolar planets.

6.4. Silicate Clouds

Brown dwarfs are expected to have clouds in their photospheres as their temperatures drop below the condensation curves of various species (Lunine et al. 1986, 1989; Tsuji et al. 1996; Chabrier et al. 2000; Ackerman & Marley 2001). There are several lines of evidence for clouds in brown dwarfs, including:

1. The red colors of L-type brown dwarfs, which quickly transition to blue colors as the brown dwarfs cool through the L-to-T transition and clouds are theorized to sink below the visible atmosphere (Kirkpatrick et al. 1999; Allard et al. 2001; Saumon & Marley 2008).
2. The variability seen in brown dwarfs (Artigau et al. 2009; Metchev et al. 2015), which is most prominent near the L-to-T transition and can be modeled with patchy clouds (Burgasser et al. 2002; Saumon & Marley 2008; Radigan et al. 2012; Apai et al. 2013).
3. The match in temperature between condensation curves and kinks in brown dwarf color–magnitude diagrams (Fegley & Lodders 1994; Lodders 1999; Morley et al. 2012; Leggett et al. 2015).

There are also alternative explanations for the previous phenomena, such as temperature–pressure profiles that have been perturbed by disequilibrium chemistry (Tremblin et al. 2015).

Solid-state spectroscopic features can be unambiguous signatures of clouds. At VHS 1256 b’s temperature, the most prominent feature is expected to be from silicate particles,

which have a broad $10 \mu\text{m}$ feature that is commonly seen in the interstellar medium and in the disks of young stars (Draine & Lee 1984). Using the Spitzer Infrared Spectrograph, Cushing et al. (2006) detected a “plateau”-shaped absorption feature from 9 to $11 \mu\text{m}$ in the spectra of several mid-L brown dwarfs, which they attributed to small amorphous silicate particles. A compendium of all of the Spitzer spectra of brown dwarfs shows that silicate features are common, but not ubiquitous, for L2–L8 brown dwarfs (Suárez & Metchev 2022).

The JWST/MIRI spectrum of VHS 1256 b shows a prominent silicate feature compared to the Spitzer brown dwarfs, with a shape that is well matched to 2M2224–0158 (see Figure 11). Burningham et al. (2021) modeled the spectrum of 2M2224–0158 and found the best fit with clouds composed of submicron enstatite/silicate, quartz, and iron. The presence of a prominent silicate feature in VHS 1256 b is strong evidence for small particles. Detailed modeling of the cloud composition and grain-size distribution will be the subject of a future paper.

Various groups have developed models for clouds in brown dwarfs and exoplanets, but they tend to focus on fitting the near-infrared ($1\text{--}2 \mu\text{m}$) part of the spectrum, where extinction from large particles ($10\text{--}100 \mu\text{m}$) mutes the spectral features (Chabrier et al. 2000; Allard et al. 2001; Saumon & Marley 2008; Madhusudhan et al. 2011). It has long been known (e.g., from the comet literature), small particles contribute less to extinction (Gao et al. 2018), but they result in a much more prominent $8\text{--}12 \mu\text{m}$ silicate feature (Min et al. 2004). JWST’s broad wavelength coverage allows us to constrain both populations of cloud particles.

7. Summary

VHS 1256 b has several qualities that distinguish it from the typical brown dwarfs that form the L-to-T sequence shown in Figure 1:

1. VHS 1256 b is a young, low-mass object that has the characteristic red colors seen in other low-gravity objects (see Sections 1 and 6.1).
2. VHS 1256 b has the largest amplitude of variability of any substellar object to date (see Section 6.2).

3. VHS 1256 b shows disequilibrium chemistry caused by turbulent, vertical mixing (see Section 6.3).
4. VHS 1256 b has a prominent silicate feature indicating the presence of small cloud particles (see Section 6.4).

Previous works have drawn physical connections between some of these qualities. Young, low-mass brown dwarfs have red colors (Faherty et al. 2016; Liu et al. 2016). These same objects are more likely to have large amplitude variability (Biller et al. 2015; Lew et al. 2016; Vos et al. 2017, 2019; Bowler et al. 2020) and to show disequilibrium chemistry (Barman et al. 2011; Zahnle & Marley 2014; Miles et al. 2018). Cloud models predict that turbulence and vertical mixing produce differentiated clouds with small particles at the top (Ackerman & Marley 2001; Helling et al. 2006; Helling & Woitke 2006; Gao et al. 2018), and objects that are reddened by extinction from large grains are more likely to have 10 μm silicate features from small grains (Suárez & Metchev 2022). Turbulent mixing is also likely to induce variability for objects of VHS 1256 b’s temperature, which are expected to have cloudy and cloud-free regions (Radigan et al. 2012; Apai et al. 2013). Together, these properties paint a picture of a highly dynamic atmosphere, where turbulent convection drives both disequilibrium chemistry and the upwelling of condensable gases, which form patchy silicate clouds that drive planetary variability.








8. Conclusions

We reduced JWST NIRSpec IFU and MIRI MRS early-release science observations of VHS 1256 b to produce the best spectrum of a planetary-mass object to date at medium resolution covering 0.97–19.8 μm . The sensitivity (NIRSpec: SNR \sim 50–400, MIRI: SNR \sim 7–20) and broad wavelength coverage of the data enabled the identification of several medium-resolution features such as water, methane, carbon monoxide, carbon dioxide, and silicate clouds within the atmosphere of VHS 1256 b. The data have sufficient S/N for forward-modeling analysis to estimate the cloudiness, chemical abundance profiles, and strength of atmospheric mixing of VHS 1256 b. Our best attempt at matching the 0.97 μm –19.8 μm spectra required combining two relatively thick cloud decks (90% $f_{\text{sed}} = .6$ and 10% $f_{\text{sed}} = 1$), low surface gravity ($\log(g) = 4.5$), a radius of 1.27 R_{Jup} , and an effective temperature of 1100 K. The derived K_{zz} profile of VHS 1256 b changes from $10^8 \text{ cm}^2 \text{ s}^{-1}$ to $10^9 \text{ cm}^2 \text{ s}^{-1}$, with stronger mixing generally occurring lower in the atmosphere. The best-attempt model matches the overall shape of the spectrum but does not adequately capture molecular absorption features typically used to estimate K_{zz} . The luminosity of VHS 1256 b was measured to within less than a percent ($\log(L_{\text{bol}}/L_{\odot}) = -4.55 \pm 0.009$), robustly providing an upper-mass limit of 20 M_{Jup} for VHS 1256 b. These initial results from the JWST early-release science observations are groundbreaking and also obtainable for numerous other nearby brown dwarfs that will be observed in future observation cycles. This observatory will be a trailblazer, pushing our understanding of atmospheric physics in planetary companions, brown dwarfs, and exoplanets for years to come.

This project was supported by a grant from STScI (JWST-ERS- 01386) under NASA contract NAS5-03127. This work benefited from the 2022 Exoplanet Summer Program in the

Other Worlds Laboratory (OWL) at the University of California, Santa Cruz, a program funded by the Heising-Simons Foundation. M.B. acknowledges support in France from the French National Research Agency (ANR) through project grant ANR-20-CE31-0012. This project has received funding from the European Research Council (ERC) under the European Union’s Horizon 2020 research and innovation program (COBREX; grant agreement n° 885593; EPIC, grant agreement n° 819155). This work has benefited from The UltracoolSheet at <http://bit.ly/UltracoolSheet>, maintained by Will Best, Trent Dupuy, Michael Liu, Rob Siverd, and Zhoujian Zhang, and developed from compilations by Dupuy & Liu (2012), Dupuy & Kraus (2013), Liu et al. (2016), and Best et al. (2018, 2021). S.-P acknowledges the support of ANID—Millennium Science Initiative Program—NCN19_171. S.M. is supported by a Royal Society University Research Fellowship. C.D. acknowledges financial support from the State Agency for Research of the Spanish MCIU through the “Center of Excellence Severo Ochoa” award to the Instituto de Astrofísica de Andalucía (SEV-2017-0709) and the Group project Ref. PID2019-110689RB-I00/AEI/10.13039/50110 0011033. B.B acknowledges funding by the UK Science and Technology Facilities Council (STFC) grant no. ST/M001229/1.

ORCID iDs

Brittany E. Miles  <https://orcid.org/0000-0002-5500-4602>
 Beth A. Biller  <https://orcid.org/0000-0003-4614-7035>
 Polychronis Patapis  <https://orcid.org/0000-0001-8718-3732>
 Kadin Worthen  <https://orcid.org/0000-0002-5885-5779>
 Emily Rickman  <https://orcid.org/0000-0003-4203-9715>
 Kielan K. W. Hoch  <https://orcid.org/0000-0002-9803-8255>
 Andrew Skemer  <https://orcid.org/0000-0001-6098-3924>
 Marshall D. Perrin  <https://orcid.org/0000-0002-3191-8151>
 Niall Whiteford  <https://orcid.org/0000-0001-8818-1544>
 Christine H. Chen  <https://orcid.org/0000-0002-8382-0447>
 B. Sargent  <https://orcid.org/0000-0001-9855-8261>
 Sagnick Mukherjee  <https://orcid.org/0000-0003-1622-1302>
 Caroline V. Morley  <https://orcid.org/0000-0002-4404-0456>
 Sarah E. Moran  <https://orcid.org/0000-0002-6721-3284>
 Mickael Bonnefoy  <https://orcid.org/0000-0001-5579-5339>
 Simon Petrus  <https://orcid.org/0000-0003-0331-3654>
 Aarynn L. Carter  <https://orcid.org/0000-0001-5365-4815>
 Elodie Choquet  <https://orcid.org/0000-0002-9173-0740>
 Sasha Hinkley  <https://orcid.org/0000-0001-8074-2562>
 Kimberly Ward-Duong  <https://orcid.org/0000-0002-4479-8291>
 Jarron M. Leisenring  <https://orcid.org/0000-0002-0834-6140>
 Maxwell A. Millar-Blanchaer  <https://orcid.org/0000-0001-6205-9233>
 Shrishmoy Ray  <https://orcid.org/0000-0003-2259-3911>
 Steph Sallum  <https://orcid.org/0000-0001-6871-6775>
 Karl R. Stapelfeldt  <https://orcid.org/0000-0002-2805-7338>
 Jordan M. Stone  <https://orcid.org/0000-0003-0454-3718>
 Jason J. Wang  <https://orcid.org/0000-0003-0774-6502>
 Olivier Absil  <https://orcid.org/0000-0002-4006-6237>
 William O. Balmer  <https://orcid.org/0000-0001-6396-8439>
 Anthony Boccaletti  <https://orcid.org/0000-0001-9353-2724>
 Mariangela Bonavita  <https://orcid.org/0000-0002-7520-8389>

Mark Booth <https://orcid.org/0000-0001-8568-6336>
 Brendan P. Bowler <https://orcid.org/0000-0003-2649-2288>
 Gael Chauvin <https://orcid.org/0000-0003-4022-8598>
 Valentin Christiaens <https://orcid.org/0000-0002-0101-8814>
 Thayne Currie <https://orcid.org/0000-0002-7405-3119>
 Camilla Danielski <https://orcid.org/0000-0002-3729-2663>
 Jonathan J. Fortney <https://orcid.org/0000-0002-9843-4354>
 Julien H. Girard <https://orcid.org/0000-0001-8627-0404>
 Alexandra Z. Greenbaum <https://orcid.org/0000-0002-7162-8036>
 Thomas Henning <https://orcid.org/0000-0002-1493-300X>
 Dean C. Hines <https://orcid.org/0000-0003-4653-6161>
 Markus Janson <https://orcid.org/0000-0001-8345-593X>
 Paul Kalas <https://orcid.org/0000-0002-6221-5360>
 Jens Kammerer <https://orcid.org/0000-0003-2769-0438>
 Grant M. Kennedy <https://orcid.org/0000-0001-6831-7547>
 Matthew A. Kenworthy <https://orcid.org/0000-0002-7064-8270>
 Pierre Kervella <https://orcid.org/0000-0003-0626-1749>
 Ben W. P. Lew <https://orcid.org/0000-0003-1487-6452>
 Michael C. Liu <https://orcid.org/0000-0003-2232-7664>
 Bruce Macintosh <https://orcid.org/0000-0003-1212-7538>
 Sebastian Marino <https://orcid.org/0000-0002-5352-2924>
 Mark S. Marley <https://orcid.org/0000-0002-5251-2943>
 Christian Marois <https://orcid.org/0000-0002-4164-4182>
 Elisabeth C. Matthews <https://orcid.org/0000-0003-0593-1560>
 Brenda C. Matthews <https://orcid.org/0000-0003-3017-9577>
 Dimitri Mawet <https://orcid.org/0000-0002-8895-4735>
 Michael W. McElwain <https://orcid.org/0000-0003-0241-8956>
 Stanimir Metchev <https://orcid.org/0000-0003-3050-8203>
 Michael R. Meyer <https://orcid.org/0000-0003-1227-3084>
 Paul Molliere <https://orcid.org/0000-0003-4096-7067>
 Eric Pantin <https://orcid.org/0000-0001-6472-2844>
 Isabel Rebollido <https://orcid.org/0000-0002-4388-6417>
 Bin B. Ren <https://orcid.org/0000-0003-1698-9696>
 Glenn Schneider <https://orcid.org/0000-0002-4511-5966>
 Malavika Vasist <https://orcid.org/0000-0002-4511-3602>
 Mark C. Wyatt <https://orcid.org/0000-0001-9064-5598>
 Yifan Zhou <https://orcid.org/0000-0003-2969-6040>
 Zackery W. Briesemeister <https://orcid.org/0000-0002-1764-2494>
 Marta L Bryan <https://orcid.org/0000-0002-6076-5967>
 Per Calissendorff <https://orcid.org/0000-0002-5335-0616>
 Faustine Cantalloube <https://orcid.org/0000-0002-3968-3780>
 Gabriele Cugno <https://orcid.org/0000-0001-7255-3251>
 Matthew De Furio <https://orcid.org/0000-0003-1863-4960>
 Trent J. Dupuy <https://orcid.org/0000-0001-9823-1445>
 Samuel M. Factor <https://orcid.org/0000-0002-8332-8516>
 Jacqueline K. Faherty <https://orcid.org/0000-0001-6251-0573>
 Michael P. Fitzgerald <https://orcid.org/0000-0002-0176-8973>
 Kyle Franson <https://orcid.org/0000-0003-4557-414X>
 Eileen C. Gonzales <https://orcid.org/0000-0003-4636-6676>
 Callie E. Hood <https://orcid.org/0000-0003-1150-7889>
 Alex R. Howe <https://orcid.org/0000-0002-4884-7150>
 Adam L. Kraus <https://orcid.org/0000-0001-9811-568X>

Masayuki Kuzuhara <https://orcid.org/0000-0002-4677-9182>
 Kellen Lawson <https://orcid.org/0000-0002-6964-8732>
 Cecilia Lazzoni <https://orcid.org/0000-0001-7819-9003>
 Pengyu Liu <https://orcid.org/0000-0001-7047-0874>
 Jorge Llop-Sayson <https://orcid.org/0000-0002-3414-784X>
 Raquel A. Martinez <https://orcid.org/0000-0001-6301-896X>
 Johan Mazoyer <https://orcid.org/0000-0002-9133-3091>
 Sascha P. Quanz <https://orcid.org/0000-0003-3829-7412>
 Jea Adams Redai <https://orcid.org/0000-0002-4489-3168>
 Matthias Samland <https://orcid.org/0000-0001-9992-4067>
 Joshua E. Schlieder <https://orcid.org/0000-0001-5347-7062>
 Motohide Tamura <https://orcid.org/0000-0002-6510-0681>
 Xianyu Tan <https://orcid.org/0000-0003-2278-6932>
 Taichi Uyama <https://orcid.org/0000-0002-6879-3030>
 Arthur Vigan <https://orcid.org/0000-0002-5902-7828>
 Johanna M. Vos <https://orcid.org/0000-0003-0489-1528>
 Kevin Wagner <https://orcid.org/0000-0002-4309-6343>
 Schuyler G. Wolff <https://orcid.org/0000-0002-9977-8255>
 Marie Ygouf <https://orcid.org/0000-0001-7591-2731>
 Xi Zhang <https://orcid.org/0000-0002-8706-6963>
 Keming Zhang <https://orcid.org/0000-0002-9870-5695>
 Zhoujian Zhang <https://orcid.org/0000-0002-3726-4881>

References

- Ackerman, A. S., & Marley, M. S. 2001, *ApJ*, 556, 872
 Allard, F., Hauschildt, P. H., Alexander, D. R., Tamanai, A., & Schweitzer, A. 2001, *ApJ*, 556, 357
 Allers, K. N., & Liu, M. C. 2013, *ApJ*, 772, 79
 Apai, D., Nardiello, D., & Bedin, L. R. 2021, *ApJ*, 906, 64
 Apai, D., Radigan, J., Buenzli, E., et al. 2013, *ApJ*, 768, 121
 Apai, D., Karalidi, T., Marley, M. S., et al. 2017, *Sci*, 357, 683
 Argyriou, I., Wells, M., Glasse, A., et al. 2020, *A&A*, 641, A150
 Artigau, É., Bouchard, S., Doyon, R., & Lafrenière, D. 2009, *ApJ*, 701, 1534
 Baraffe, I., Homeier, D., Allard, F., & Chabrier, G. 2015, *A&A*, 577, A42
 Barman, T. S., Macintosh, B., Konopacky, Q. M., & Marois, C. 2011, *ApJ*, 733, 65
 Best, W. M. J., Liu, M. C., Magnier, E. A., & Dupuy, T. J. 2021, *AJ*, 161, 42
 Best, W. M. J., Magnier, E. A., Liu, M. C., et al. 2018, *ApJS*, 234, 1
 Biller, B. A., Vos, J., Bonavita, M., et al. 2015, *ApJL*, 813, L23
 Biller, B. A., Vos, J., Buenzli, E., et al. 2018, *AJ*, 155, 95
 Boccaletti, A., Lagage, P. O., Baudoz, P., et al. 2015, *PASP*, 127, 633
 Boccaletti, A., Cossou, C., Baudoz, P., et al. 2022, *A&A*, 667, A165
 Bohlin, R. C., Hubeny, I., & Rauch, T. 2020, *AJ*, 160, 21
 Böker, T., Arribas, S., Lützgendorf, N., et al. 2022, *A&A*, 661, A82
 Bowler, B. P., Zhou, Y., Morley, C. V., et al. 2020, *ApJL*, 893, L30
 Burgasser, A. J., Kirkpatrick, J. D., Liebert, J., & Burrows, A. 2003, *ApJ*, 594, 510
 Burgasser, A. J., Marley, M. S., Ackerman, A. S., et al. 2002, *ApJL*, 571, L151
 Burningham, B., Faherty, J. K., Gonzales, E. C., et al. 2021, *MNRAS*, 506, 1944
 Burrows, A., Marley, M., Hubbard, W. B., et al. 1997, *ApJ*, 491, 856
 Chabrier, G., Baraffe, I., Allard, F., & Hauschildt, P. 2000, *ApJ*, 542, 464
 Charbonneau, D., Knutson, H. A., Barman, T., et al. 2008, *ApJ*, 686, 1341
 Chauvin, G., Lagrange, A. M., Dumas, C., et al. 2004, *A&A*, 425, L29
 Currie, T., Burrows, A., Itoh, Y., et al. 2011, *ApJ*, 729, 128
 Cushing, M. C., Rayner, J. T., & Vacca, W. D. 2005, *ApJ*, 623, 1115
 Cushing, M. C., Roellig, T. L., Marley, M. S., et al. 2006, *ApJ*, 648, 614
 Draine, B. T., & Lee, H. M. 1984, *ApJ*, 285, 89
 Dupuy, T. J., & Kraus, A. L. 2013, *Sci*, 341, 1492
 Dupuy, T. J., & Liu, M. C. 2012, *ApJS*, 201, 19
 Dupuy, T. J., Liu, M. C., Evans, E. L., et al. 2022, *MNRAS*, 519, 1688
 Dupuy, T. J., Liu, M. C., Magnier, E. A., et al. 2020, *RNAAS*, 4, 54
 Faherty, J. K., Riedel, A. R., Cruz, K. L., et al. 2016, *ApJS*, 225, 10
 Fegley, B. J., & Lodders, K. 1994, *Icar*, 110, 117
 Filippazzo, J. C., Rice, E. L., Faherty, J., et al. 2015, *ApJ*, 810, 158

- Fortney, J. J., Lodders, K., Marley, M. S., & Freedman, R. S. 2008, *ApJ*, **678**, 1419
- Fortney, J. J., Marley, M. S., & Barnes, J. W. 2007, *ApJ*, **659**, 1661
- Fortney, J. J., Marley, M. S., Lodders, K., Saumon, D., & Freedman, R. 2005, *ApJL*, **627**, L69
- Gaia Collaboration, Brown, A. G. A., Vallenari, A., et al. 2021, *A&A*, **649**, A1
- Galicher, R., Marois, C., Macintosh, B., Barman, T., & Konopacky, Q. 2011, *ApJL*, **739**, L41
- Gao, P., Marley, M. S., & Ackerman, A. S. 2018, *ApJ*, **855**, 86
- Gauza, B., Béjar, V. J. S., Pérez-Garrido, A., et al. 2015, *ApJ*, **804**, 96
- Glasse, A., Rieke, G. H., Bauwens, E., et al. 2015, *PASP*, **127**, 686
- Gordon, K. D., Bohlin, R., Sloan, G. C., et al. 2022, *AJ*, **163**, 267
- Green, J. J., Beichman, C., Basinger, S. A., et al. 2005, *Proc. SPIE*, **5905**, 185
- Grillmair, C. J., Burrows, A., Charbonneau, D., et al. 2008, *Natur*, **456**, 767
- Helling, C., Thi, W. F., Woitke, P., & Fridlund, M. 2006, *A&A*, **451**, L9
- Helling, C., & Woitke, P. 2006, *A&A*, **455**, 325
- Hinkley, S., Carter, A. L., Ray, S., et al. 2022, *PASP*, **134**, 095003
- Hinz, P. M., Rodigas, T. J., Kenworthy, M. A., et al. 2010, *ApJ*, **716**, 417
- Hoch, K. K. W., Konopacky, Q. M., Barman, T. S., et al. 2022, *AJ*, **164**, 155
- Hubeny, I., & Burrows, A. 2007, *ApJ*, **669**, 1248
- Karalidi, T., Marley, M., Fortney, J. J., et al. 2021, *ApJ*, **923**, 269
- Kirkpatrick, J. D. 2005, *ARA&A*, **43**, 195
- Kirkpatrick, J. D., Reid, I. N., Liebert, J., et al. 1999, *ApJ*, **519**, 802
- Kirkpatrick, J. D., Reid, I. N., Liebert, J., et al. 2000, *AJ*, **120**, 447
- Knutson, H. A., Charbonneau, D., Allen, L. E., Burrows, A., & Megeath, S. T. 2008, *ApJ*, **673**, 526
- Konopacky, Q. M., Barman, T. S., Macintosh, B. A., & Marois, C. 2013, *Sci*, **339**, 1398
- Krist, J. E., Balasubramanian, K., Beichman, C. A., et al. 2009, *Proc. SPIE*, **7440**, 74400W
- Leggett, S. K., Morley, C. V., Marley, M. S., & Saumon, D. 2015, *ApJ*, **799**, 37
- Lew, B. W. P., Apai, D., Zhou, Y., et al. 2016, *ApJL*, **829**, L32
- Liu, M. C., Dupuy, T. J., & Allers, K. N. 2016, *ApJ*, **833**, 96
- Lodders, K. 1999, *ApJ*, **519**, 793
- Lodders, K., & Fegley, B. 2002, *Icar*, **155**, 393
- Lunine, J. I., Hubbard, W. B., Burrows, A., Wang, Y. P., & Garlow, K. 1989, *ApJ*, **338**, 314
- Lunine, J. I., Hubbard, W. B., & Marley, M. S. 1986, *ApJ*, **310**, 238
- Madhusudhan, N., Burrows, A., & Currie, T. 2011, *ApJ*, **737**, 34
- Marley, M. S., Ackerman, A. S., Cuzzi, J. N., & Kitzmann, D. 2013, in *Comparative Climatology of Terrestrial Planets*, ed. S. J. Mackwell et al. (Tucson, AZ: Univ. Arizona Press), 367
- Marley, M. S., Saumon, D., Cushing, M., et al. 2012, *ApJ*, **754**, 135
- Marley, M. S., Saumon, D., Guillot, T., et al. 1996, *Sci*, **272**, 1919
- Marley, M. S., Saumon, D., Visscher, C., et al. 2021, *ApJ*, **920**, 85
- Marois, C., Macintosh, B., Barman, T., et al. 2008, *Sci*, **322**, 1348
- Marois, C., Zuckerman, B., Konopacky, Q. M., Macintosh, B., & Barman, T. 2010, *Natur*, **468**, 1080
- McGovern, M. R., Kirkpatrick, J. D., McLean, I. S., et al. 2004, *ApJ*, **600**, 1020
- Metchev, S. A., Heinze, A., Apai, D., et al. 2015, *ApJ*, **799**, 154
- Miles, B. E., Skemer, A. J., Barman, T. S., Allers, K. N., & Stone, J. M. 2018, *ApJ*, **869**, 18
- Min, M., Dominik, C., & Waters, L. B. F. M. 2004, *A&A*, **413**, L35
- Morley, C. V., Fortney, J. J., Marley, M. S., et al. 2012, *ApJ*, **756**, 172
- Morley, C. V., Marley, M. S., Fortney, J. J., et al. 2014, *ApJ*, **787**, 78
- Morzinski, K. M., Males, J. R., Skemer, A. J., et al. 2015, *ApJ*, **815**, 108
- Mukherjee, S., Batalha, N. E., Fortney, J. J., & Marley, M. S. 2023, *ApJ*, **942**, 71
- Noll, K. S., Geballe, T. R., Leggett, S. K., & Marley, M. S. 2000, *ApJL*, **541**, L75
- Patten, B. M., Stauffer, J. R., Burrows, A., et al. 2006, *ApJ*, **651**, 502
- Perrin, M. D., Sivaramakrishnan, A., Lajoie, C.-P., et al. 2014, *Proc. SPIE*, **9143**, 91433X
- Petrus, S., Chauvin, G., Bonnefoy, M., et al. 2023, *A&A*, **670**, L9
- Radigan, J., Jayawardhana, R., Lafrenière, D., et al. 2012, *ApJ*, **750**, 105
- Rajan, A., Rameau, J., De Rosa, R. J., et al. 2017, *AJ*, **154**, 10
- Rich, E. A., Currie, T., Wisniewski, J. P., et al. 2016, *ApJ*, **830**, 114
- Rigby, J., Perrin, M., McElwain, M., et al. 2022, arXiv:2207.05632
- Saumon, D., & Marley, M. S. 2008, *ApJ*, **689**, 1327
- Saumon, D., Marley, M. S., Cushing, M. C., et al. 2006, *ApJ*, **647**, 552
- Skemer, A. J., Close, L. M., Szűcs, L., et al. 2011, *ApJ*, **732**, 107
- Skemer, A. J., Hinz, P. M., Esposito, S., et al. 2012, *ApJ*, **753**, 14
- Skemer, A. J., Marley, M. S., Hinz, P. M., et al. 2014, *ApJ*, **792**, 17
- Sorahana, S., & Yamamura, I. 2012, *ApJ*, **760**, 151
- Stone, J. M., Skemer, A. J., Kratter, K. M., et al. 2016, *ApJL*, **818**, L12
- Suárez, G., & Metchev, S. 2022, *MNRAS*, **513**, 5701
- Tremblin, P., Amundsen, D. S., Mourier, P., et al. 2015, *ApJL*, **804**, L17
- Tsuji, T., Ohnaka, K., & Aoki, W. 1996, *A&A*, **305**, L1
- Tsuji, T., Yamamura, I., & Sorahana, S. 2011, *ApJ*, **734**, 73
- Vos, J. M., Allers, K. N., & Biller, B. A. 2017, *ApJ*, **842**, 78
- Vos, J. M., Faherty, J., Gagné, J., et al. 2022, *BAAS*, **54**, 102.206
- Vos, J. M., Biller, B. A., Bonavita, M., et al. 2019, *MNRAS*, **483**, 480
- Wells, M., Pel, J. W., Glasse, A., et al. 2015, *PASP*, **127**, 646
- Zahnle, K. J., & Marley, M. S. 2014, *ApJ*, **797**, 41
- Zhou, Y., Bowler, B. P., Apai, D., et al. 2022, *AJ*, **164**, 239
- Zhou, Y., Bowler, B. P., Morley, C. V., et al. 2020, *AJ*, **160**, 77